# Examining a Year-Long Chemical Degradation Process and Reaction Kinetics in Pristine and Defect-Passivated Lead Halide Perovskites

Parth Raval, Mohammad Ali Akhavan Kazemi, Julie Ruellou, Julien Trébosc, Olivier Lafon, Laurent Delevoye, Frédéric Sauvage, G. Manjunatha Reddy

# Examining year-long chemical degradation process and reaction kinetics in pristine and defect-passivated lead halide perovskites

Parth Raval,[a] Mohammad Ali Akhavan Kazemi,[b] Julie Ruellou,[b] Julien Trébosc,[c] Olivier Lafon,[a] Laurent Delevoye,[a] Frédéric Sauvage,[b] and G. N. Manjunatha Reddy [a]*

[a] *University of Lille, CNRS, Centrale Lille Institut, Univ. Artois, UMR 8181−UCCS− Unité de Catalyse et Chimie du Solide, F-59000, Lille, France*

[b] *Laboratoire de Réactivité et Chimie des Solides (LRCS), UMR CNRS 7314 - Institut de Chimie de Picardie FR 3085, Université de Picardie Jules Verne, 33 rue Saint Leu, FR-80039 Amiens Cedex, France.*

[c] *University of Lille, CNRS, INRAE, Centrale Lille, Univ. Artois, FR 2638 - IMEC - Institut Michel-Eugène Chevreul, F-59000 Lille, France*

*corresponding author: gnm.reddy@univ-lille.fr

TOC graphic

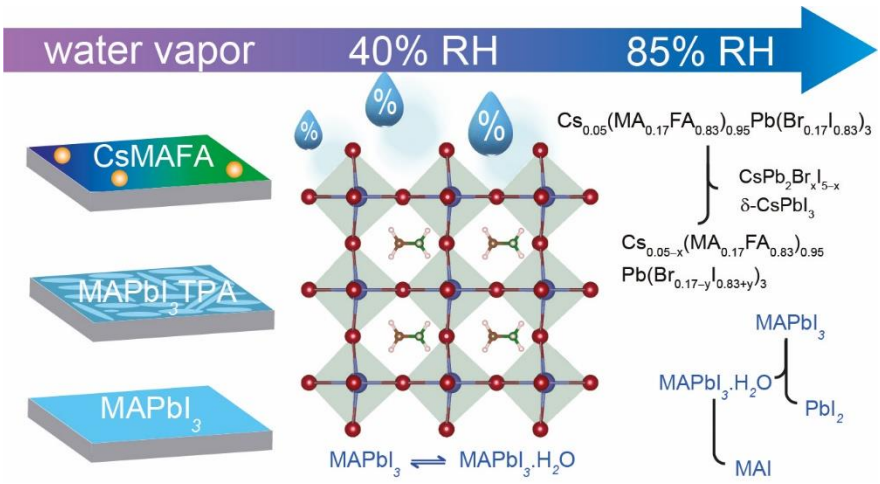

**Abstract**

As a promising solar energy harvesting technology, solution-processed metal halide perovskites (MHPs) are of great current interest in developing low-cost and efficient photovoltaic cells. Despite their excellent optoelectronic properties and the nascent advancements in composition tailoring and interfacial engineering to develop high performance MHPs, issues associated with the long-term environmental stability of these materials are yet to be addressed. We examine the moisture-induced cascade degradation reactions over a year for methylammonium lead iodide ($MAPbI_3$) and formamidinium-rich ($Cs_{0.05}(MA_{0.17}FA_{0.83})_{0.95}Pb(Br_{0.17}I_{0.83})_3$) formulations at 40% and 85% relative humidity (RH) in the air. The transformative reactions at 85% RH accelerates the chemical degradation process in both MA-rich and FA-rich perovskites, yielding to the different organic and inorganic byproducts within a few hours, but the exposure to 40% RH retains the longevity of these materials up to several months. The defect passivation by tetrapropylammonium cation ($TPA^+$) imparts enhanced stability of $MAPbI_3$ particles, irrespective of the exposure conditions to water vapor. By resolving thin film morphology at sub-nanometer to nanometer resolution using solid-state (ss)NMR spectroscopy and X-ray diffraction (XRD) techniques, kinetics of degradation reactions and structural insights into the inorganic/organic interfaces and degradation products are obtained and compared. Our findings provide mechanistic details into the cascade degradation reactions in pristine and defect passivated MHPs, and provide guidelines for novel passivating and interfacial engineering strategies to further improve robustness of the MHPs with respect to environmental stressors.

**Introduction**

Solution-processed $ABX_3$-type metal halide perovskites (MHPs) are crystalline semiconducting materials, whereby the monovalent organic/inorganic cation (A) occupies the cubo-octahedral voids of the inorganic $BX_6$ framework. Lead halide perovskites have garnered interest in a wide range of optoelectronic applications, including light emitters, photocatalysts, and laser devices, and these materials are also among the highest-performing perovskite solar cells (PSCs). Single junction lead halide perovskite solar cells have demonstrated power conversion efficiencies (PCE) of over 25%.[1–4] Within the recent past, developments have been sought by means of compositional tailoring of A-/X-site ions and interfacial engineering of the device layers, enabling such PCE values to be achieved in perovskite photovoltaics.[5–8] However, the solar cell efficiency rapidly decreases in the presence of light, moisture, and temperature. The soft ionic lattice of 3D hybrid perovskites is sensitive to these external stimuli, which leads to chemical degradation of these materials and the associated photovoltaic device layers.[9–11] Specifically, 'A' site and 'X' site ion lability caused by these external stressors is hypothesized to contribute to the perovskite degradation. Recently, studies have showed that the photoinduced halide migration occurs in perovskite lattice and 'A' site cation lability triggered by water molecules in the vapor also affects the stability of corner-shared $PbI_xBr_{6-x}$ octahedra.[12,13] Efforts to address the environmental stability of these materials are at the forefront today.[14,15] Among the extrinsic factors that influence the stability, the presence of oxygen and water vapor drastically reduces the solar cell performance due to moisture-assisted transformative reactions depending on the water vapor concentration in the air, i.e., relative humidity, RH. For example, protocols have been suggested to examine the moisture-induced degradation pathways of MHPs at (i) low relative humidity (< 40% RH) and (ii) high relative humidity (>70% RH) in the air, in order to assess the environmental stability of solar cell modules.[16,17]

Methylammonium lead iodide ($MAPbI_3$) and formamidinium lead iodide ($FAPbI_3$) have been widely used in developing high-performance perovskite solar cells (PSCs) due to the favorable bandgap and high charge carrier mobility in these materails.[18–20] The tolerance factor modulation by mixing ions of different sizes has been shown to enhance the phase stability of the corner-sharing perovskite phase.[21,22] For example, FA-rich formulation involving methylammonium ($MA^+$), formamidinium ($FA^+$), and cesium ($Cs^+$) at the 'A' site ($Cs_{0.05}(FA_{0.83}MA_{0.17})_{0.95}Pb(Br_{0.17}I_{0.83})_3$) have led to improved environmental stability as well as solar cell performance,[23] and mixed halide perovskite compositions such as iodide, bromide, and chloride anions aid in bandgap tunability.[24,25] However, recent studies indicate that the multi-cation/anion formulations also undergo degradation in the presence of external stimuli, though the transformative reaction is deliberately slower compared to the single-cation/anion compositions.[26–29] In another approach to enhance the longevity of the hybrid perovskites, dimensional tailoring of perovskites into mixed-dimensional 2D/3D phases or layered perovskite slabs separated by the large spacer cations that cannot be incorporated in the cubo-octahedral voids has primarily been explored. The alkyl-ammonium cations such as butylamine (BA)[30], phenylethylammonium (PEA)[31], and aminovaleric acid iodide (AVAI)[32] form layered perovskites, and the hydrophobic nature of the organic spacer cations impede the degradation in the presence of moisture. Notably, layered 2D/ quasi-2D Ruddlesden-Popper phases[33,34] and Dion-Jacobson phases[35] provide enhanced environmental stability. Consequently, the large insulating organic layers lead to quantum-well structures that reduce the charge transport across the perovskite layers whereas broadening the optical bandgap, thus causing a lowering of the device's PCE compared to conventional 3D perovskites.[36]

Passivation of point defects in $MAPbI_3$, $FAPbI_3$, and mixed-cation formulation(s) has been used in conjunction with interfacial engineering of perovskite layer and contact layers to suppress non-radiative charge carrier recombination, enabling high stability and PCE of about 24%.[37–41] It can be achieved by incorporating small-molecule additives into the perovskite precursor solution during the film deposition, which leads to defect passivation of perovskite grains or by depositing layers of passivating agents on the perovskite thin films.[42,43] A wide variety of supramolecular chemistry approaches and molecular modulators for perovskite solar cells have been proposed to achieve defect passivation and environmental stability.[44–46] For example, Lewis base tetrapropylammonium cation ($TPA^+$) passivated $MAPbI_3$ solar cells (non-encapsulated devices) exhibited a PCE of 18.7% with a $T_{80}$ of 250 h, i.e., device operation time with 80% of original efficiency retained.[47] FA-rich formulation passivated with thiophene-based ligands allowed PCE values of over 24% to be achieved with enhanced stability ($T_{80}$~3570h) and longevity of solar cell devices.[41] To this end, an atomic-scale understanding of the thin film morphology, microstructure, and intermolecular interactions between the passivating agents and perovskite grains is crucially important to develop interfacial engineering strategies and novel passivation ligands. Although the outdoor operational stability of perovskite solar cells has been widely studied by tracking the photophysical properties and power conversion efficiency as functions of light, temperature or moisture, a detailed understanding of the morphological and structural changes that contribute to the degradation/transformation reactions in different layers and interfaces between them is lacking. Various analytical techniques have been used to probe the instability of $MAPbI_3$ and $FAPbI_3$-based perovskites, including X-ray diffraction (XRD), thermogravimetry, mass spectrometry, optical or electron microscopy, ssNMR spectroscopy and theoretical calculations.[48–54] Only a handful of studies have used atomic-scale characterization techniques to characterize the different

degradation products and their kinetic pathways, specifically for assimilating the long-term environmental stability of several months.[15,51,54–57] It can be due, at least in part, to the limitations associated with the spatial and temporal resolution of analytical techniques to probe the accurate chemical nature of intermediates, short-lived species at minuscule concentrations in cascading degradation pathways. Nonetheless, the role of moisture on the thin film morphology, grain size, and long-range structural order can be obtained by electron microscopy and X-ray diffraction (XRD) techniques.[58] However, examining the degradation pathways by means of organic A-site cations and passivating ligands is less straightforward by using long-range techniques.[59] To this end, the short-range nature associated with ssNMR facilitates the changes in local structures and intermolecular interactions to be elucidated and distinguished. Owing to its complementary length scale and ability to probe atomic-level interactions, ssNMR spectroscopy has been increasingly used to characterize photoabsorbers, contact layers and the interfaces between them.[59–75]

Here, we examine one year-long moisture-induced degradation reactions in $MAPbI_3$, defect-passivated $MAPbI_3$, and FA-rich CsMAFA perovskite thin films at complementary length scales using XRD and ssNMR techniques. The reaction kinetics of cascade reactions and the associated degradation products are analyzed and compared. Specifically, the role of water vapor concentration in the air (40% RH and 85% RH) on the instability of these materials are accessed. The evolution of metastable species, interconversion between them, and the formation of different inorganic/organic byproducts are systematically characterized by XRD and 2D ssNMR spectroscopy technique. In addition, an overview of the different degradation reactions in MA, FA, and Cs-based perovskites and their cation/anion alloys characterized in the study are compared with the degradation products reported in the literature studies. A comprehensive stability

assessment provided in this study has much wider relevance, for example, to develop interfacial engineering strategies to enhance the environmental stability of hybrid perovskites.

## Experimental section

*Materials and sample preparation*. For $MAPbI_3$ thin films, the precursor solution was prepared by dissolving 1 mol/L methylammonium iodide (MAI) (159 mg), 1 mol/L $PbI_2$ (461 mg) in anhydrous N, N-dimethylformamide (Sigma-Aldrich), and anhydrous dimethylsulfoxide (Sigma-Aldrich) with a 4:1 v/v ratio, respectively. The solution was kept at 70 °C overnight under stirring and then cooled down to ambient temperature. The solution was spin-coated (MBraun SC210) on a glass substrate according to a two-step procedure inside an Ar-filled glovebox (MBraun Unilab Pro SP), first at 1000 rpm for 10 s and 4000 rpm for 20 seconds. During the second step, 1 mL of toluene as an anti-solvent was dropped 10 s before the end of the program. These films were annealed at 110 °C for 30 min inside the glovebox to crystallize the perovskite structure leading to a mirror-like dark film. For $TPA^+$ passivated $MAPbI_3$, stoichiometric 4 mol.% of tetrapropylammonium iodide (TPAI) was utilized to substitute MAI. For the preparation of CsMAFA thin films, the CsMAFA precursor solution was prepared by dissolving 1.1 $mol.L^{-1}$ $PbI_2$ (508 mg), 0.22 $mol.L^{-1}$ $PbBr_2$ (80.7 mg), 1 $mol.L^{-1}$ FAI (172 mg), 0.20 $mol.L^{-1}$ MABr (22.4 mg), and 0.06 $mol.L^{-1}$ CsI (17.5 mg) in anhydrous N,N-dimethylformamide (Sigma-Aldrich) and anhydrous dimethyl sulfoxide (Sigma-Aldrich) with 4:1 ratio (v/v), respectively.

The different inorganic Cs lead halides were synthesized using the following procedure.[57] To obtain $CsPb_2Br_5$ powder, a crystallization reaction between lead bromide (1.4 mmol) and cesium bromide (0.7 mmol) was carried out. First, these compounds were dissolved in 6 mL of HBr (HBr,

48%, Fisher chemicals), and the resultant mixture was heated at 118 °C and stirred overnight, and then allowed to cool down at room temperature. The precipitate was collected after a vacuum filtration, washed by diethyl ether, and dried under vacuum at 60 °C. The different cesium lead Br/I alloys were synthesized by using the same crystallization method by varying the stoichiometric ratios of the precursor salts, $PbI_2$:$PbBr_2$:CsBr:CsI, in HBr. Starting from $CsPb_2Br_5$, $CsPb_2I_5$ was synthesized using a halogen exchange reaction under inert atmosphere using controlled flow of argon gas through the Schlenk line. The equimolar $CsPb_2Br_5$ and lead iodide ($PbI_2$) powders was mixed with 21 mL of ternary solvent mixture consisting of 1-octadecene (20 mL, obtained from Alfa Aesar, 90%), oleic acid (0.5 mL, Alfa Aesar, 90%) and oleylamine (0.5 mL, Sigma-Aldrich, 70%). The reaction mixture was heated at 160 °C for overnight, and allowed to cool down to room temperature. The final product was collected after vacuum filtration, by washing with ethyl ether, and dried at 60 °C (4 h in vacuum) and sintered at 160 °C (30 min). However, the halogen exchange may not occur efficiently during this process, in order to obtain pure $CsPb_2I_5$ phase, leading the formation of other byproducts.

*Moisture exposure conditions.* Powders of pristine and defect-passivated perovskite materials (obtained by scratching thin films) were dispersed on glass petri dishes and stored in a glass desiccator, where the relative humidity (RH, water vapor concentration in the air) was maintained at 40±5%. For the exposure to moisture at 85±5% RH in the air, the particles spread on the petri dishes were placed in a humidity-controlled hydration chamber, whereby a beaker containing saturated KCl solution was used in a desiccator to generate 85% RH, as examined by a hygrometer placed inside the desiccator. In both cases, the glass desiccators were stored in the dark and at 23 °C. These materials were taken out at specific time intervals for *ex situ* ssNMR studies. During the

sample packing into the rotors and unpacking process (~5 minutes each), the samples were exposed to laboratory illumination (500-700 Lux) and moderate humidity (50-60% RH).

*X-ray Diffraction.* Thin films deposited in glass substrates were used for the XRD measurements. X-ray diffraction patterns of thin films were acquired *in situ* by Bruker D8 diffractometer with a Cu-$K_\alpha$ source ($\lambda_{CuKa1}$ = 1.54056 Å and $\lambda_{CuKa2}$ = 1.54439 Å), equipped with a LynxEye detector. Each diffraction pattern was acquired from $2\theta$ = 7° - 40° with a step size of 0.01°.

*Solid-state NMR spectroscopy.* Samples for solid-state NMR analysis were prepared in an identical manner to solar cell fabrication. Pristine and passivated perovskite material was spin-coated to glass substrates, and powders of these materials were obtained by scratching off the spin-coated thin films. The samples were then packed either into a Bruker 1.3 mm or 2.5 mm rotor, or into Phoenix 1.6 mm rotors. All 1D $^{1}$H MAS and 2D $^{1}$H-$^{1}$H correlation NMR experiments on pristine and moisture-exposed perovskites were carried out on a Bruker Avance Neo (18.8 T, $^{1}$H Larmor frequency = 800.1 MHz) spectrometer. Detailed acquisition parameters corresponding to the 2D $^{1}$H-$^{1}$H double-quantum–single-quantum correlation and $^{1}$H-$^{1}$H spin diffusion NMR experiments are given in Supporting Information (Section 1, Tables S1-S7). The $^{1}$H chemical shifts were calibrated with respect to neat TMS using the $^{1}$H signal of adamantane at 1.8 ppm as a secondary external reference. $^{133}$Cs chemical shifts were calibrated with respect to 0.1 mol.L$^{-1}$ CsCl solution.

**Results and discussion**

**Impact of water vapor on the structure of $MAPbI_3$ thin film.** In order to probe the changes in crystallinity and short-range structure before and after exposure to moisture at 85% RH in the air, we combined X-ray diffraction and ssNMR spectroscopy techniques. These results are presented in Figure 1, whereby the changes are observed by means of XRD patterns as well as the $^{1}$H NMR

chemical shifts are plotted. The morphological features of pristine and defected passivated $MAPbI_3$ thin films are presented in supporting information (Figure S1), which exhibit favorable morphology with grain sizes in the sub-micron to micron range, akin to the morphology of photoactive layers in high efficiency perovskite photovoltaic devices. First, we discuss the changes in the long-range crystallinity to identify the intermediate species and final byproducts by analyzing the XRD patterns (Figure 1a). In the XRD patterns of the fresh material, peaks at 14.1°, 20.0°, 23.4°, 24.4°, 28.4°, and 31.8° correspond to (110), (200), (211), (202), (220), and (310) diffraction planes of the tetragonal structure of the $MAPbI_3$ perovskite (space group: I4/mcm). Upon exposure to moisture for 48h, reflections at 8.1°, 10.5°, and 12.6° corresponding to the (001) and (-101) planes of the mono-hydrated perovskite ($MAPbI_3.H_2O$) and (001) plane of $PbI_2$, respectively, are observed, consistently with the previous observations.[51,54,76] To identify the peaks corresponding to the different degradation products, the experimental powder patterns of fresh and aged $MAPbI_3$ materials are compared with the simulated power patterns of the $MAPbI_3$, $MAPbI_3.H_2O$ and $PbI_2$ (supporting information, Figure S2), in order to assess the phase purity of the fresh material and the different degradation products. While these results confirm the formation of crystalline hydrate and inorganic $PbI_2$, the organic degradation products, such as methyl ammonium iodide (MAI), are not detected in XRD due to the lack of long-range order or low concentration of MAI species or both, thus highlighting the limitation of this technique to probe degradation reactions in hybrid perovskites.

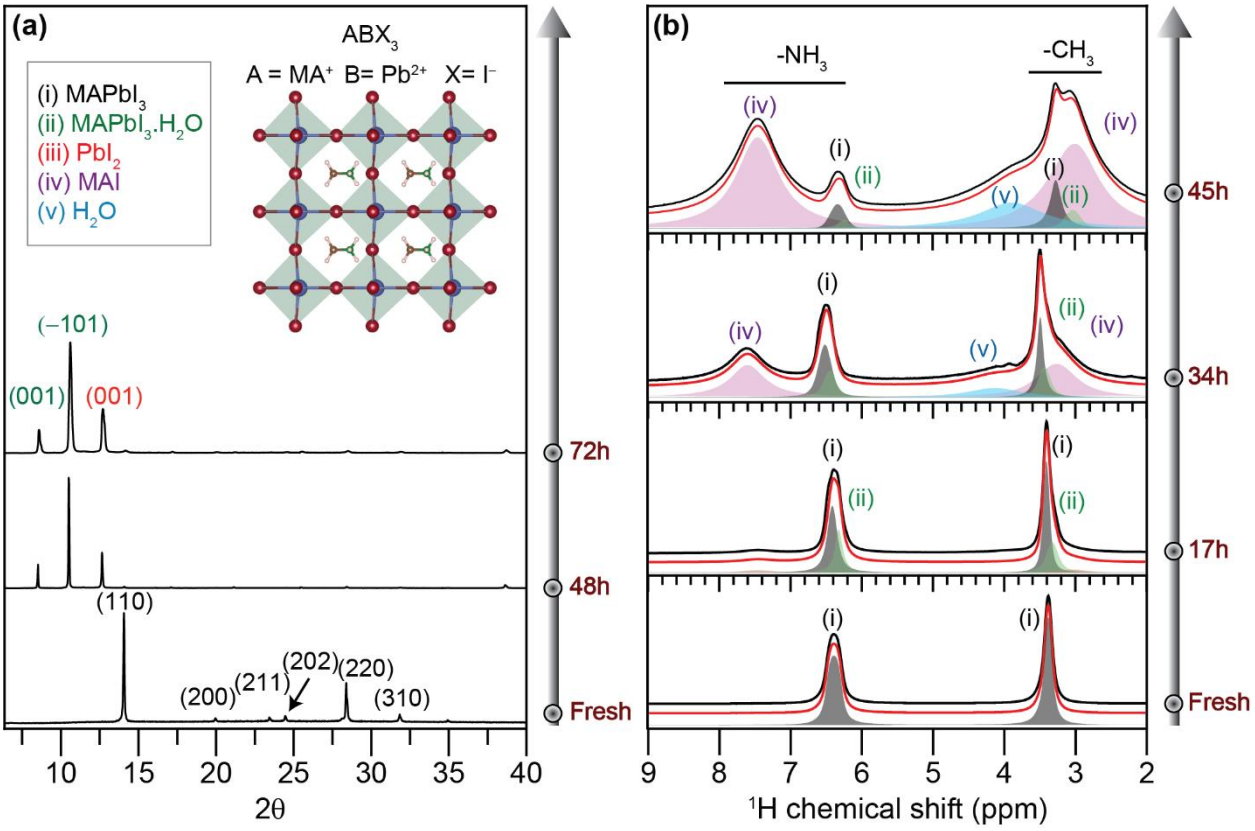


**Figure 1.** (a) XRD patterns of $MAPbI_3$ before and after exposure to moisture (85% RH) for different durations as indicated. The peaks are labelled corresponding to Bragg planes of $MAPbI_3$ (i, black), $MAPbI_3.H_2O$ (ii, green), and $PbI_2$ (iii, red) are presented, and the crystal structure of $MAPbI_3$ is shown in the inset. (b) Experimental 1D $^1H$ MAS NMR spectra of $MAPbI_3$ before and after exposure to moisture (85% RH) presented with deconvolution analysis of peak intensities of four species: $MAPbI_3$ (i, black), $MAPbI_3.H_2O$ (ii, green), MAI (iv, magenta) exhibiting signals of $NH_3^+$ and $CH_3$ groups, and $H_2O$ (v, turquoise). The deconvoluted intensities associated with different degradation products are indicated in Table 1. All XRD patterns were acquired with the $MAPbI_3$ thin film spin coated on glass substrates, and the $^1H$ NMR spectra were acquired for scratched thin films at 18.8 T ($^1H$ = 800.1 MHz) and at room temperature.

The solid-state 1D $^1H$ NMR spectrum of the fresh $MAPbI_3$ (Figure 1b) exhibits two signals at 6.4 and 3.4 ppm attributed to $NH_3^+$ and $CH_3$ groups of methylammonium cation. In agreement with

the XRD results and analysis, subtle differences in the $^{1}H$ lineshapes of $NH_3^+$ and $CH_3$ sites in moisture-exposed material (17h at 85% RH) are attributable to the formation of $MAPbI_3.H_2O$ as characterized by 2D $^{1}H$-$^{1}H$ correlation NMR spectra (Figure S3), however, the water resonance is not observed at this exposure time.[54] Intriguingly, the observation of low-intensity signals at 3.0 and 7.6 ppm indicate the formation of trace amounts of methyl ammonium iodide (MAI). To corroborate this analysis, a $^{1}H$ NMR spectrum of neat MAI is acquired and compared (Supporting Information, Figure S4). The integrated intensities of simulated $^{1}H$ spectra enable the relative molar fractions of pristine $MAPbI_3$, its monohydrate ($MAPbI_3.H_2O$), and MAI to be estimated, which are 60% (black), 32% (green), and 8% (magenta), respectively (Figure 2). Further exposure to moisture at 85% RH increases the formation of MAI, which is evident from the higher-intensity peaks at 3.0 and 7.6 ppm. Spectral deconvolution analysis indicates that the MAI molar fraction has increased from 8% to 47% after 34 h and 65% after 45 h. After exposure to moisture for 34 h, an additional broad peak at ~4.0 ppm emerged, which could be hypothesized to originate from either a different form of hydrated $MAPbI_3$/poorly crystalline PbIOH as previously observed or surface adsorbed water molecules.[54] These observations are strikingly important to understand the degradation pathways as well as reaction kinetics influenced by water molecules, the concentration of which in the vapor plays a crucial role in the degradation process. The kinetic aspects of the cascade degradation of reactions can be examined by the spatial and temporal resolution enabled by the XRD and solid-state NMR techniques combined at complementary length scales. Specifically, XRD analysis provides insights into the formation of crystalline phases such as $MAPbI_3.H_2O$ and $PbI_2$. This analysis reveals that approximately half of the $MAPbI_3$ transformed into its hydrate and/or $PbI_2$/MAI, allowing the half-life decay of the pristine $MAPbI_3$ films estimated to be in the range of 10-20h. However, the remaining degradation reaction process

occurs at a relatively slower rate, and the transformation of $MAPbI_3$ to its degraded products takes a few days to complete. It is consistent with our previous study, whereby the kinetics of transformative reactions in $FAPbI_3$ occurs at different rates in hybrid perovskites with different half-lives of the photo absorbers, further confirming that the kinetics of degradation reactions strongly depends on the concentration of water molecules in the vapour.[77] To test this, we studied the moisture-induced degradation reaction of the same $MAPbI_3$ material after exposure to 40% RH using $^1H$ NMR spectroscopy.

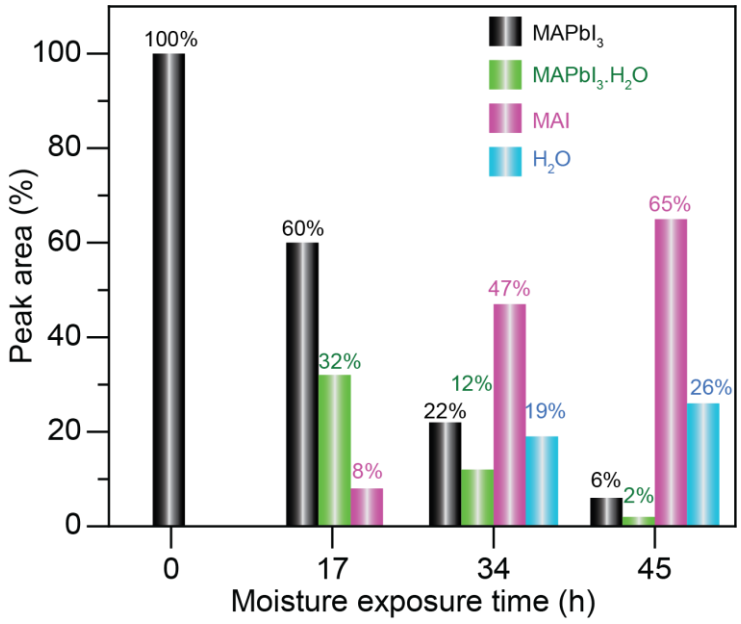


**Figure 2.** A plot of proton peak intensities of $MAPbI_3$ as a function of moisture exposure time for the different by products formed, which are color coded as depicted in the inset.

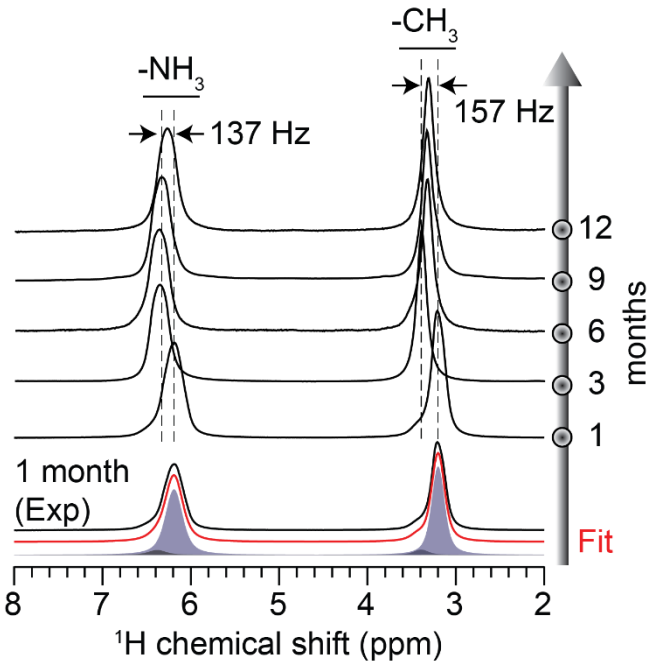


**Figure 3.** Solid-state 1D $^{1}$H NMR spectra of $MAPbI_3$ powder scratched from thin films deposited on glass substrates before and after exposure to moisture at 40% RH. All spectra were acquired at 18.8 T ($^{1}$H, 800.1 MHz) and room temperature.

Figure 3 presents 1D $^{1}$H MAS NMR spectra of $MAPbI_3$ after exposure to moisture at 40% RH, which showed subtle changes in the resonant frequencies within the linewidth. Unlike 85% RH, for which MAI was detected after 34 h, there are no spectral features corresponding to MAI even after exposure to moisture at 40% RH for up to a year. However, subtle changes in the peak positions $\Delta\delta(^{1}H)$ = 157 Hz (within the $^{1}$H linewidths) and $\Delta\delta(NH_3\text{-}CH_3)$ = 3.0, 2.8, 3.1, 3.1 and 3.0 ppm (bottom to top) are observed, which is due to the interconversion between the $MAPbI_3$ and its hydrated $MAPbI_3.H_2O$.[54] The formation of $MAPbI_3$ monohydrate has previously been studied using XRD techniques.[54,78] In addition, the 2D $^{1}$H-$^{1}$H correlation spectroscopy resolves the different $^{1}$H chemical shifts hidden in the linewidths, indicating the formation of two different

$MAPbI_3$ phases.[54] Based on these experimental results, the lineshape of a 1D $^1H$ NMR spectrum is deconvoluted in to the separate signals corresponding to $MAPbI_3.H_2O$ and $MAPbI_3$ species. It is noteworthy that accurate kinetic studies of the cascade degradation reactions require the time-resolved XRD and NMR data to be more frequently acquired and analyzed, in order to construct kinetics plots from which the order of the reactions can be extracted and compared. In addition, the reaction kinetic and the half-lives of the reactants depend on the concentration of water molecules in the vapor.

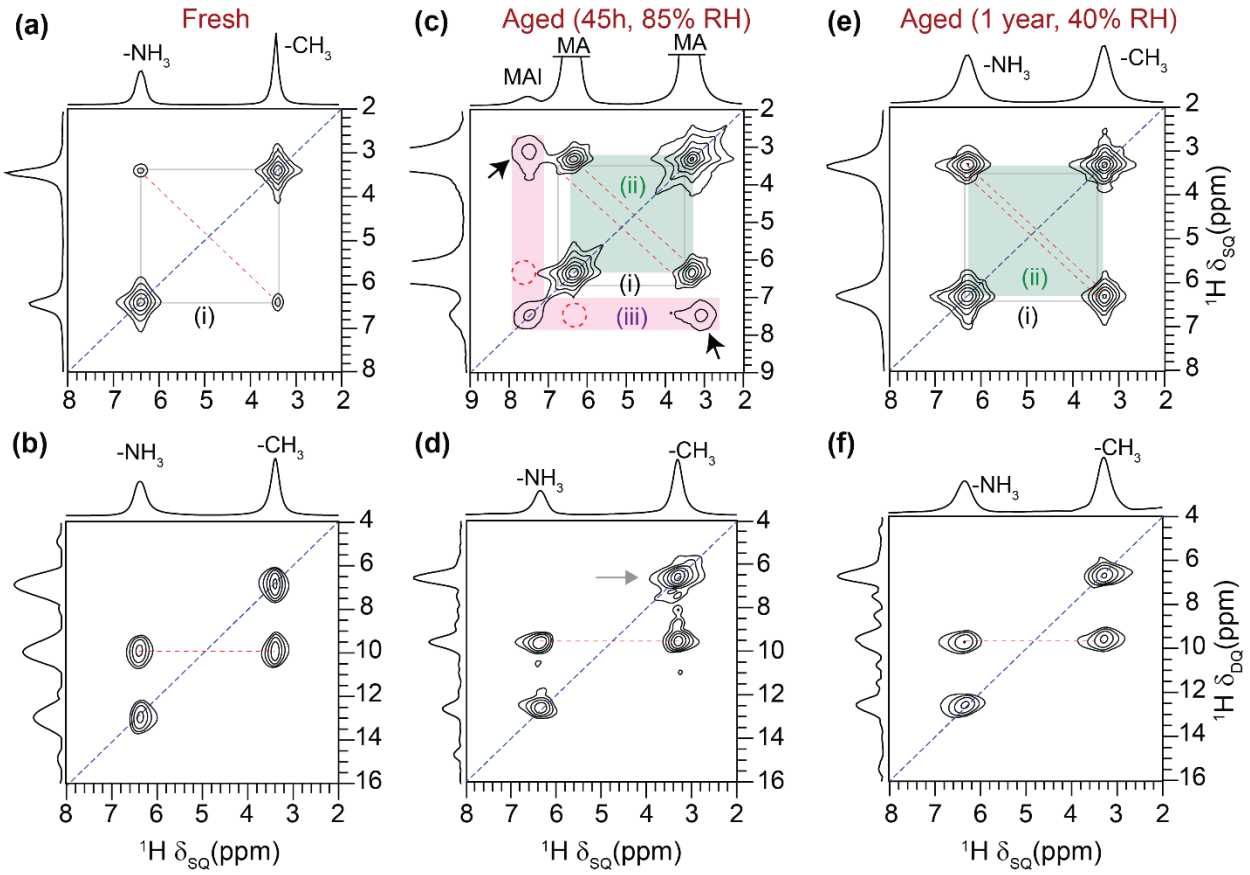


**Figure 4.** Solid-state 2D $^1H$-$^1H$ spin-diffusion (top) and DQ-SQ correlation (bottom) NMR spectra of $MAPbI_3$ thin film acquired before (a, b) and after exposure to moisture: (c, d) at 85% RH and (e, f) at 40% RH, respectively. All the spectra are acquired at 18.8 T ($^1H$, 800.1 MHz) and room

temperature, using powders obtained by scratching the thin films deposited on a glass substrate. Peaks corresponding to the different byproducts are color coded as depicted in Figure 1.

To resolve the $^{1}$H peaks corresponding to the different degradation products, we carried out 2D $^{1}$H-$^{1}$H correlation NMR experiments. Given the low sample mass (approximately a milligram of powder obtained by scratching the thin films) and longer spin-lattice ($T_1$) relaxation times of up to 30 seconds associated with these materials, the 2D correlation experiments require longer acquisition times of the order several hours, which limits the temporal resolution of 2D ssNMR to examine the kinetics of degradation reactions. Nonetheless, 2D spectra of these materials before and after moisture exposure were acquired and compared to identify the peaks corresponding to the different degradation products and their local structures. We applied $^{1}$H-$^{1}$H spin-diffusion (SD) and double-quantum–single-quantum (DQ-SQ) correlation experiments to characterize organic cations and different degradation products in $MAPbI_3$. These experiments produce 2D peaks for closely proximate and through-space dipolar coupled H-H pairs at sub-nanometer distances, which shed light on the formation of different byproducts, their local structures and interactions. In a 2D SD experiment, spin magnetization exchange occurs between the chemically inequivalent proton sites in MA cations, yielding off-diagonal peaks. For fresh $MAPbI_3$ (Figure 4a), the off-diagonal peaks between 3.4 and 6.4 ppm indicate the magnetization exchange between the methyl and ammonium protons, as highlighted by the grey rectangle. In addition, the DQ peaks can be excited for $^{1}$H-$^{1}$H spin pairs (< 5 Å) in methyl and ammonium groups of $MA^+$, which are detected at the sum of SQ frequencies along the indirect (vertical) dimension of the 2D DQ-SQ correlation spectrum (Figure 4b). The on-diagonal DQ peak at 3.4 + 3.4 = 6.8 ppm and 6.4 + 6.4 = 12.8 ppm corresponds to $^{1}$H sites in the methyl and ammonium groups of $MA^+$ cations, respectively. The off-diagonal DQ peak at 3.4 + 6.4 = 9.8 ppm along the indirect dimension is due to intramolecular $^{1}$H-$^{1}$H dipolar interactions between methyl protons and ammonium protons.

For the aged $MAPbI_3$ (85% RH, 45h), the $^1H$-$^1H$ spin-diffusion spectrum (Figure 4c, S5) displays diagonal and cross peaks corresponding to the $MAPbI_3$ (grey rectangle) and its hydrate (green box), as well the peaks at 7.5 and 3.0 ppm associated with the ammonium and methyl groups of MAI (magenta), respectively. The absence of cross-peaks between the $MAPbI_3$ and MAI moieties (red circles) indicates that these moieties are not molecularly intermingled within the same domains/grains, rather spatially distributed into the different domains. The DQ-SQ spectrum (Figure 4d) of the same material shows peaks that are akin to what is observed in $MAPbI_3$ with subtle distortions in the $CH_3$ peak (grey arrow), indicating the formation of $MAPbI_3$ hydrate, however, 2D peaks for MAI are undetected due to the lack of long-range order. The 2D peaks originating from the $MAPbI_3.H_2O$ are detected with higher intensities when the $MAPbI_3$ is exposed to 85% RH for 17h, as indicated in the supporting information (Figure S3 displays an additional set of on-diagonal DQ signals at 6.6 ppm and 12.6 ppm, which shows the presence of $MA^+$ cations in different local chemical environments).[54] This analysis confirms that the water vapor concentration plays a detrimental role in the degradation kinetic as well the types and concentrations of the different byproducts. To confirm this, similar experiments and analyses were carried out after exposure to $MAPbI_3$ for over a year at a relatively low water vapor concentration (45% RH). The 2D $^1H$-$^1H$ SD and DQ-SQ spectra (Figure 4e, 4f) of aged $MAPbI_3$ (40% RH, 1 year) do not display the peaks corresponding to MAI, consistently with the analysis of 1D $^1H$ NMR spectra presented above. However, a broadening of the diagonal and cross peaks due to the formation of the solid solution of the $MAPbI_3.H_2O$ phase is observed.[76] Key learning from this study is that the combination of XRD and ssNMR study allows the moisture-induced degradation of organic cations and inorganic species to be identified and distinguished. The observed long-term stability of $MAPbI_3$ at a low concentration of water vapor (RH $\leq$40%) is consistent with the

study by Wang et al., which showed the performance of the Ag/spiro-OMeTAD/$MAPbI_3$/$TiO_2$/FTO/glass PSCs is not significantly affected even after aging the material at 40% RH for 100 days.[79]

**Impact of defect passivation on the moisture-induced degradation of $MAPbI_3$.**

The longevity of $MAPbI_3$ thin films can be enhanced, in part, by defect passivation of grain boundaries. For example, the addition of a Lewis base tetrapropylammonium iodide (TPAI) at a low concentration (2-4 mol%) in conjunction with $PbI_2$ (9 mol%) reduces non-radiative energy losses and enhances the stability of $MAPbI_3$-based solar cells by passivation of the surface defects through $TPA^+$ and lower-dimensional $TPAPb_4I_9$ within the grain boundaries.[47] It is of particular interest to understand how the passivating agents impact the kinetics of degradation reactions in $MAPbI_3$ thin films. To examine the role of surface passivation on $MAPbI_3$ moisture-induced degradation, we acquired and compared the X-ray diffractograms and 1D/2D $^1H$ NMR spectra of $MAPbI_3$ treated with 4 mol.% of TPA passivating agent before and after the exposure to moisture at 85% RH. In the XRD plot (Figure 5a), the fresh material exhibits diffraction peaks at 14.1°, 20.0°, 23.4°, 24.4°, 28.4°, and 31.8° which are attributed to the (110), (200), (211), (202), (220), and (310) diffraction planes of the passivated $MAPbI_3$ perovskite. The lattice cell parameters are identical to $MAPbI_3$: a = 9.002(2) Å, c = 12.937(2) Å, and a cell volume V = 1048.4(2) $Å^3$, suggesting that the addition of $TPA^+$ does not lead to $MAPbI_3$ lattice expansion or shrinkage. Exposure to moisture at 85% RH for over 2 days yields a set of new diffraction peaks at 8.0°, 10.5° and 12.6° corresponding to (−101) and (001) planes of $MAPbI_3.H_2O$ and $PbI_2$.[76] Intensities of these peaks increase as a function of moisture-exposure time. Interestingly, the intensity corresponding to the (−101) plane of $MAPbI_3.H_2O$ after exposure to 72h at 85% RH in $MAPbI_3$.TPA (Figures

5a) is less intense compared to the same reflection in aged $MAPbI_3$ (72h, 85% RH) as presented in Figure 1a, indicating the enhanced stability obtained by the TPA passivation. The low intensity diffraction peak at low angle ($2\theta = 8.1°$) corresponds to the low-dimensional $TPAPb_4I_9$, which is formed at miniscule concentrations when $PbI_2$ is added during the synthesis of $MAPbI_3$.TPA, consistently with the previous study.[47] A detailed lineshape fitting analysis of the experimental powder XRD patterns of moisture aged $MAPbI_3$.TPA materials and the associated byproducts are provided in Supporting Information (Figure S6), and compared with the simulated power patterns of the $MAPbI_3$, $MAPbI_3.H_2O$ and $PbI_2$, in order to assess the phase purity of the fresh material and the different degradation products.

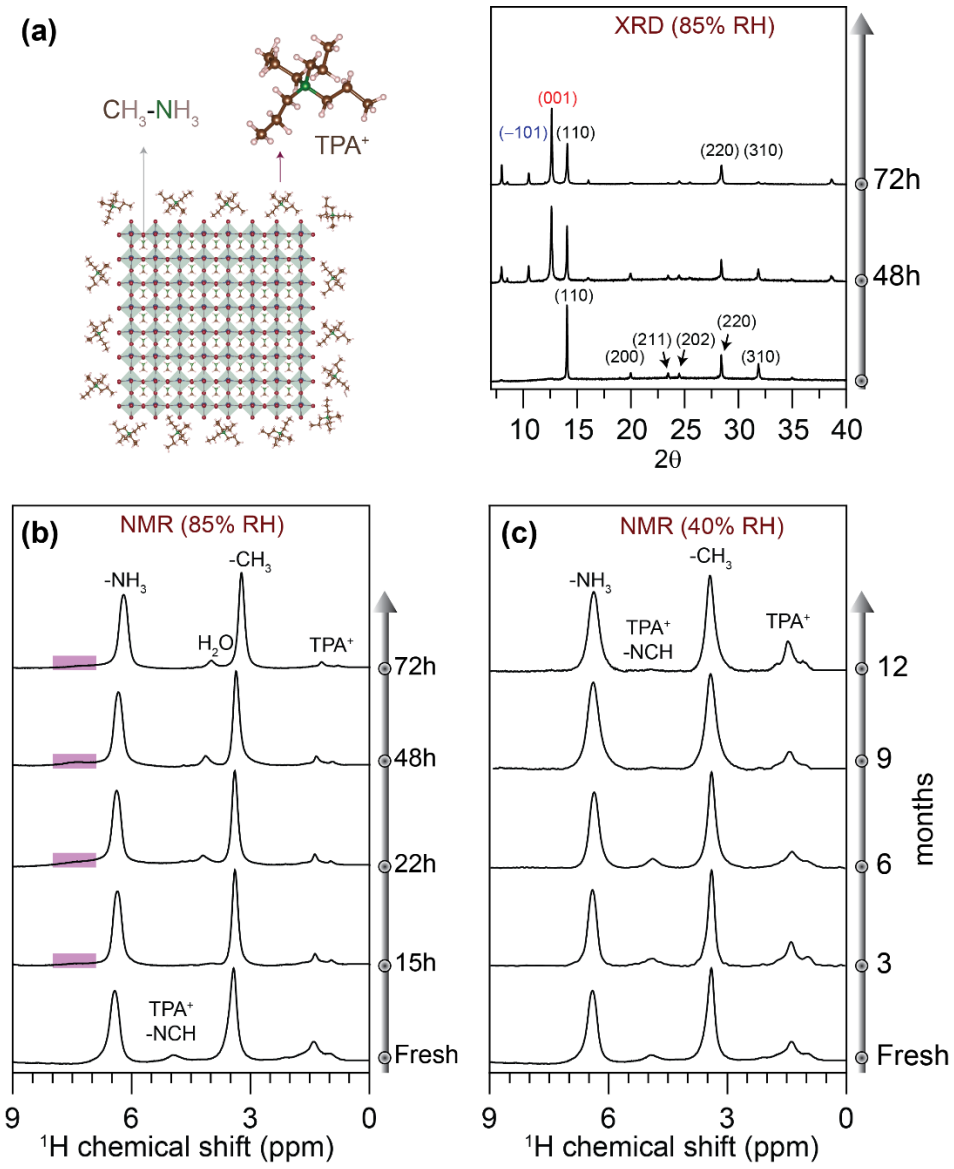


**Figure 5.** (a) XRD patterns of $MAPbI_3$.TPA (4 mol%) before and after exposure to moisture (85% RH) with Bragg reflections labelled for $MAPbI_3$ (black), $MAPbI_3.H_2O$ (green), and $PbI_2$ (red). (b) Solid-state 1D $^1H$ MAS NMR spectra of the same material before and after exposure to moisture (b) at 85% RH and (c) at 40% RH, acquired at 18.8 T ($^1H$, 800.1 MHz) and room temperature.

The complementary information on the moisture-induced degradation reactions and kinetics in $MAPbI_3$.TPA (4 mol%) can be obtained by analyzing 1D $^1H$ MAS NMR spectra (Figure 5). In the

1D $^{1}$H NMR spectrum (Figure 5b) of fresh $MAPbI_3$.TPA (4%), the strong intensity $^{1}$H peaks at 3.5 and 6.5 ppm are due to $MA^+$ cation in $MAPbI_3$, and the weak intensity signals at 4.9, 1.3, and 0.9 ppm due to the $NC^{\alpha}H_2$, $C^{\beta}H_2$ and $CH_3$ protons of $TPA^+$, respectively. The $^{1}$H NMR spectrum of neat TPAI shown in the Supporting Information (Figure S7) further corroborates the spectral analysis. After exposure to moisture (85% RH, 15h), the intensity of the $^{1}$H signals associated with $TPA^+$ cation decreases, and a new peak at 4.0 ppm emerges upon prolonged exposure. More importantly, a weak intensity peak centered at 7.3 ppm appeared in the $^{1}$H spectrum (Supporting Information, Figure S8, magnified inset) acquired after exposure to moisture for 48h, which can be ascribed to the $–NH_3^+$ peak of MAI, that is present in very low concentration, unlike what is observed in the pristine $MAPbI_3$. A low concentration of MAI is formed even after 72h exposure to 85% RH, which is estimated to be < 5%, compared to over 65% in $MAPbI_3$, suggesting that the introduction of $TPA^+$ cation enhances moisture stability and decelerates the kinetics of moisture-induced degradation reactions of $MAPbI_3$.[47,54] Likewise, the extent of water vapor concentration plays a crucial role in driving the degradation pathway forward for the same $MAPbI_3$.TPA (4mol.%) material. It is noteworthy that the $^{1}$H NMR signal of the water molecules could have a broad feature and difficult to resolve, which further depends on the concentration of water molecules. For example, water peaks are detected with much higher intensities when the materials are exposed to 85% RH for 3 days (Figures 1b and 5b) than the same material under low RH of 40%. Next, we exposed the defects passivated $MAPbI_3$.TPA (4mol.%) material to 40% RH and $^{1}$H NMR spectra were acquired at different time periods (Figure 5c). While these spectra show no particular signatures of the peaks corresponding to the degradation products, however, a broadening of the proton peaks for the $-NCH_2$ site of $TPA^+$ cation is observed after 9 months of exposure to 40% RH. More importantly, the peaks corresponding to MAI are undetected even after

1 year of exposure to 40% RH, suggesting the formation of MAI is hampered, which can be attributed as improved longevity of $MAPbI_3$-based thin films.

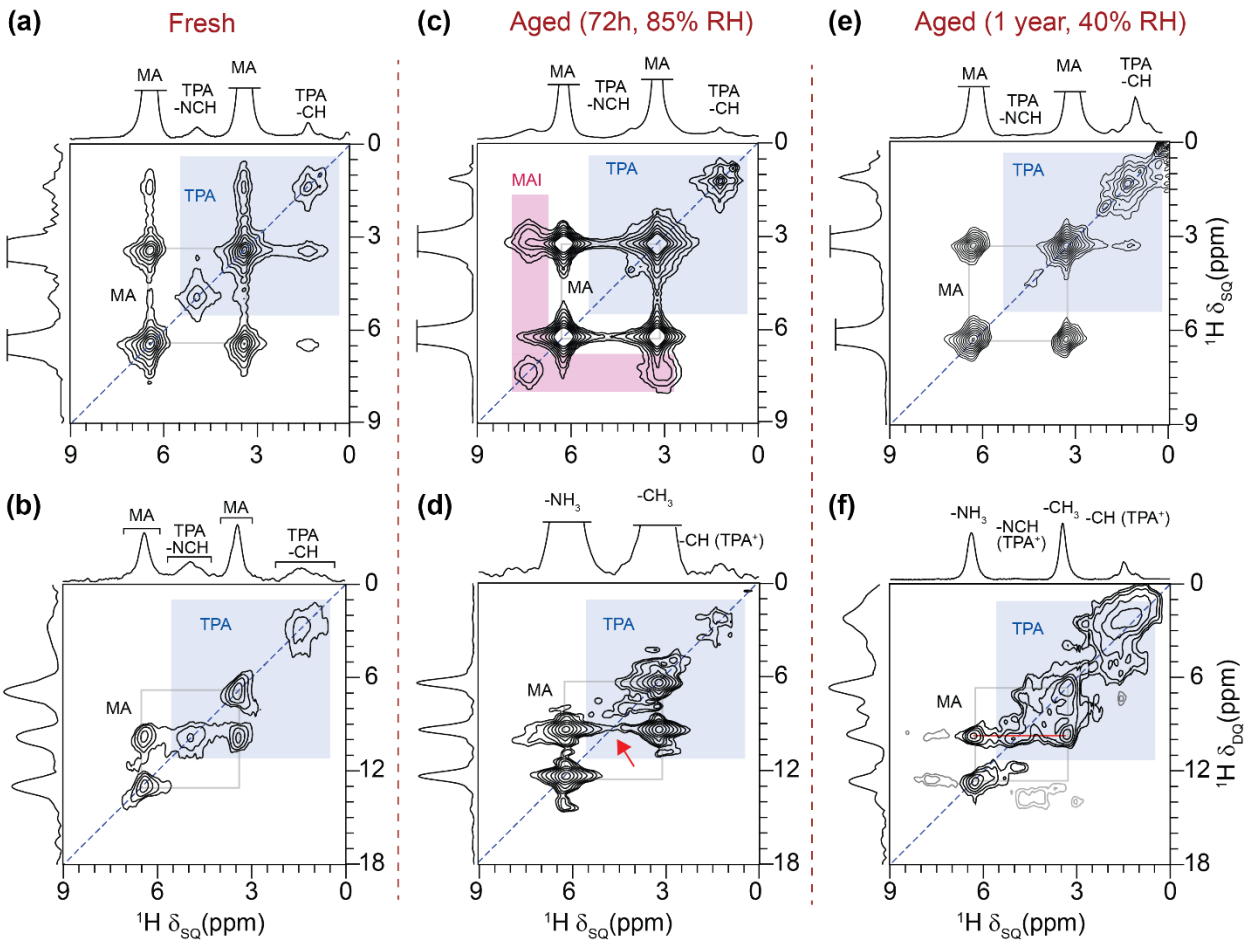


**Figure 6**. Influence of defects passivation of $MAPbI_3$ using Lewis base TPA on the degradation reactions at different water vapor concentration. Solid-state 2D $^1H$-$^1H$ spin-diffusion (top) and DQ-SQ correlation (bottom) NMR spectra of $MAPbI_3$.TPA (4mol.%). (a, b) fresh (c, d) 72h exposed, 85% RH and (e, f) 1 year aged, 40% RH, respectively, acquired at 18.8 T ($^1H$, 800.1 MHz) and room temperature. All samples for ssNMR analysis were obtained by scratching the thin films deposited on glass substrates.

Correspondingly, 2D $^{1}$H-$^{1}$H SD and DQ-SQ correlation NMR techniques and analysis (Figure 6) were applied to elucidate the local structures of $MA^{+}$ and $TPA^{+}$ cations as well as to probe the moisture-induced structural changes. Information on through-space interactions between the TPA cations and $MAPbI_3$ materials are obtained by analyzing the 2D $^{1}$H-$^{1}$H SD spectra acquired with different spin diffusion mixing times (Supporting Information, Figure S9). Analysis of 2D $^{1}$H-$^{1}$H SD spectra of fresh and aged $MAPbI_3$.TPA (4mol.%) for different exposure times to moisture are presented in supporting information (Figures S9 and S10). For fresh $MAPbI_3$.TPA (4 mol.%), the 2D $^{1}$H-$^{1}$H SD spectrum acquired with 500 ms mixing time (Figure 6a) displays strong intensity off-diagonal peaks due to intramolecular $^{1}$H-$^{1}$H dipolar interactions between methyl and ammonium proton of $MA^{+}$ cations (grey rectangle) as well as intermolecular $^{1}$H-$^{1}$H dipolar interactions between $MA^{+}$ protons and $TPA^{+}$ protons (blue shaded rectangle), corroborating the inter-molecular interactions between $TPA^{+}$ passivating agent and $MAPbI_3$. The cross-peaks between $C^{\beta}H_2$ and $NC^{\alpha}H_2$ groups of $TPA^{+}$ are not detected owing to the low concentration of these cations, which suggests that, at least in part, the $TPA^{+}$ moieties well dispersed and passivated on the $MAPbI_3$ material. If TPA cations are phases separated, then the strong cross peaks would have appeared, dur to close through-space proximities between these molecules. For the same material, Figure 6b presents the 2D $^{1}$H-$^{1}$H DQ-SQ spectrum, which shows the on-diagonal DQ peaks at 1.8 ppm, 2.6 ppm, and 9.8 ppm, stems from the short proximities between protons within methyl, $C^{\beta}H_2$, and -$NC^{\alpha}H_2$ groups of $TPA^{+}$, respectively (a detailed analysis is presented in supporting information, Section 12). After exposure to $MAPbI_3$.TPA (4 mol.%) to moisture for 72 h at 85% RH, the 2D $^{1}$H-$^{1}$H SD spectrum (Figure 6c) corroborates the decreased intensity of $TPA^{+}$ cations since the off-diagonal peaks between the $TPA^{+}$, and $MA^{+}$ signals are poorly detected. The magenta rectangle in Figure 6c highlights the emergence of MAI as it marks the cross-peaks between the

methyl and ammonium protons of MAI. However, the 2D $^{1}H$-$^{1}H$ DQ-SQ NMR spectrum (Figure 6c) shows the 2D peaks identical to those observed in the fresh sample, except the on-diagonal peak of $NC^{\alpha}H_2$ group (as shown in the red arrow). The absence of this signal is consistent with the reduced intensity of $TPA^+$ cations in the 1D spectra owing to subtle changes in its Lewis base properties in the presence of moisture. Notably, XRD analysis further corroborates these results on the long-range order by displaying the peaks corresponding to the $MAPbI_3$ phase even after exposure to moisture for 72h (Figure 5a), indicating the moisture exposure has less impact on the defect passivated $MAPbI_3$ material.

After a year of exposure to low water vapor concentration (40% RH), we acquired 2D NMR spectra (Figure 6e,f) of $MAPbI_3$.TPA (4 mol.%). While the diagonal peaks of the $NC^{\alpha}H_2$ group of the $TPA^+$ group are also not detected in the 2D $^{1}H$-$^{1}H$ SD NMR spectra (Figure 6e), a diagonal peak at 4.0 ppm which is hypothesized to be originating from the adsorbed water is detected. In addition, an off-diagonal peak between $C^{\beta}H_2$ protons of $TPA^+$ and methyl protons of $MA^+$ cations is detected. This observation indicates that some $TPA^+$ cations are located, at least in part, in close proximity to $MA^+$, however, the intensity of these off-diagonal peaks is reduced when compared to the fresh sample. In particular, the off-diagonal peaks between $MA^+$ ammonium protons and those of $TPA^+$ are poorly detected, suggesting local changes in the affinity interactions at the $MAPbI_3$ surface. These results are further corroborated by acquiring and analyzing the 2D $^{1}H$-$^{1}H$ SD spectra of fresh and moisture aged materials acquired with different mixing times, as shown in Supporting Information (Figure S9). Nevertheless, no signal corresponding to the MAI phase is detected for the aged $MAPbI_3$.TPA material (at 85% RH for 72h) as compared to the $MAPbI_3$ material (65% MAI is formed after gaining at 85% RH for 72h), indicating that the passivation by TPA moieties enhances moisture stability of the $MAPbI_3$ material. The 2D DQ-SQ correlation

spectrum of this sample (Figure 6f) exhibits the on-diagonal peaks that are reminiscent of the fresh material, but the intensities of the peaks associated with $NC^{\alpha}H_2$ groups of $TPA^+$ are decreased, and a peak broadening is observed, indicating the disorder in the local chemical environments of $TPA^+$ cations. These results confirm that the concentration of water molecules plays an important role in determining the instability of defects passivated hybrid perovskite thin films. Although the defects passivation reduces the degree of penetration of water molecules into the perovskite framework, exposure to high water concentration (85% RH) may lead to surface wettability of $TPA^+$ species, allowing the water molecules to ingress into the $MAPbI_3$ lattice leading to the formation of byproducts in the form of MAI, as detected in the 2D $^1H$-$^1H$ SD spectra (Supporting Information, Figures S9 and S10). The most significant result of this study is that the different degradation reactions and kinetics of transformative reactions as function of water vapor concentration are resolved by complementary XRD and ssNMR spectroscopy techniques.

**Moisture stability of $Cs_{0.05}(MA_{0.17}FA_{0.83})_{0.95}Pb(Br_{0.17}I_{0.83})_3$ (CsMAFA).**

The FA-rich cation alloys such as $Cs_{0.05}(MA_{0.17}FA_{0.83})_{0.95}Pb(Br_{0.17}I_{0.83})_3$ (CsMAFA) have been used to develop high-performing single-junction PSCs with PCE over 23%[80] as well as tandem devices with silicon with certified PCE of over 29%.[81] The introduction of $Cs^+$ and $FA^+$ cations is expected to enhance the thermal stability of the perovskite material.[82,83] Although the instability in $FAPbI_3$ is studied by multiscale characterization techniques, the moisture-induced degradation reactions in triple cation CsMAFA are seldom studied.[57,84] Changes in the local structures of A-site cations such as $Cs^+$, $MA^+$, and $FA^+$ in this formulation can be investigated by ssNMR spectroscopy. Specifically, the high sensitivity due to 100% isotopic natural abundance and moderate gyromagnetic ratio, $\gamma(^{133}Cs) = 0.13\ \gamma(^1H)$ and spin $I = 7/2$, and sufficiently large chemical shift dispersion associated with $^{133}Cs$ NMR enable the local chemical environments of Cs cations

in perovskite to be identified and distinguished. Here, we examine $^{133}$Cs and $^{1}$H sites to unravel the role of moisture on the morphology and stability of CsMAFA thin film before and after exposure to moisture. For the pristine CsMAFA, the $^{133}$Cs signal at ~30 ppm (Figure 7a) is ascribed to the $Cs^+$ in the CsMAFA perovskite framework. For the triple cation formulation studies, the signal is displaced from the shifts reported in the literature due to the variation in the local chemical environment in terms of neighboring halide in purely cesium-based perovskite phases.[85] For moisture-exposed CsMAFA (85% RH for ~7 days), $^{133}$Cs MAS NMR spectrum exhibits a peak at ~30 ppm as well as a distribution of peaks centered at 286 ppm, which can be attributed to the extra framework $Cs^+$ cations in Cs-based inorganic compounds.[57] To identify the plausible byproducts, we synthesized and characterized $CsPb_2Br_xI_{5-x}$ compounds ($x$ = 1-5, i.e.) using powder XRD and $^{133}$Cs MAS NMR spectroscopy. For these compounds, and the precursors used in the synthesis, powder XRD patterns are presented in Supporting Information (Figure S11), and compared with the PXRD patterns of CsMAFA before and after exposure to moisture. A detailed XRD analysis suggests that the ternary halogen-plumbate compounds such as $CsPb_2Br_5$ could be one of the byproducts formed, although the presence of analogous Cs containing lead iodide compounds cannot be merely ignored (Supporting Information, Figures S11 and S12).[85–90] For example, the existence of $CsPb_2I_5$ has recently been reported.[90] In addition, the 1D $^{133}$Cs MAS NMR spectra of these compounds exhibit $^{133}$Cs peaks in the range of 200-300 ppm (Supporting Information, Figure S13), which could be attributable to the different local chemical environments of the Cs atoms in δ-$CsPbI_3$, CsX (X= Br, I) and $Cs_4PbBr_6$.[85,91] The combined XRD and NMR analysis indicates that the $Cs^+$ cations migrate, at least in part, from the perovskite framework in order to form layered 2D perovskite formulations as well as non-perovskite phases. Although a precise chemical nature of these non-perovskite phases is difficult to establish due to dilute

concentration and the compositional and structural heterogeneity, as evidenced by the broad distribution of $^{133}Cs$ chemical shifts (200-300 ppm), we hypothesize the byproducts are among the $CsPb_2Br_xI_{5-x}$ compounds (with $x$ = 1-5), δ-$CsPbI_3$ and $PbI_2$. The partial $Cs^+$ ion leaching from the perovskite framework raises a question regarding the local changes and the distribution of the other organic cations, such as $MA^+$ and $FA^+$, in the perovskite framework. To elucidate the local structures of $MA^+$ and $FA^+$ cations in CsMAFA before and after exposure to moisture, we acquired 1D $^1H$ and 2D $^1H$-$^1H$ correlation NMR spectra. In the 1D $^1H$ NMR spectrum of the pristine CsMAFA (Figure 7b), the $MA^+$ cations produce peaks at 3.4 ppm and 6.3 ppm, respectively, and the ammonium and methylene protons of $FA^+$ resonate at 7.4 and 8.2 ppm, respectively. Upon aging at 85% RH, 1D $^1H$ NMR spectrum exhibited identical signals for $MA^+$ and $FA^+$ cations, but line narrowing for the $MA^+$ and $FA^+$ peaks is observed, which can be reasoned to the local ordering of organic cation resulting from cationic rearrangements as some of the $Cs^+$ cations leave the perovskite framework to form the byproducts.

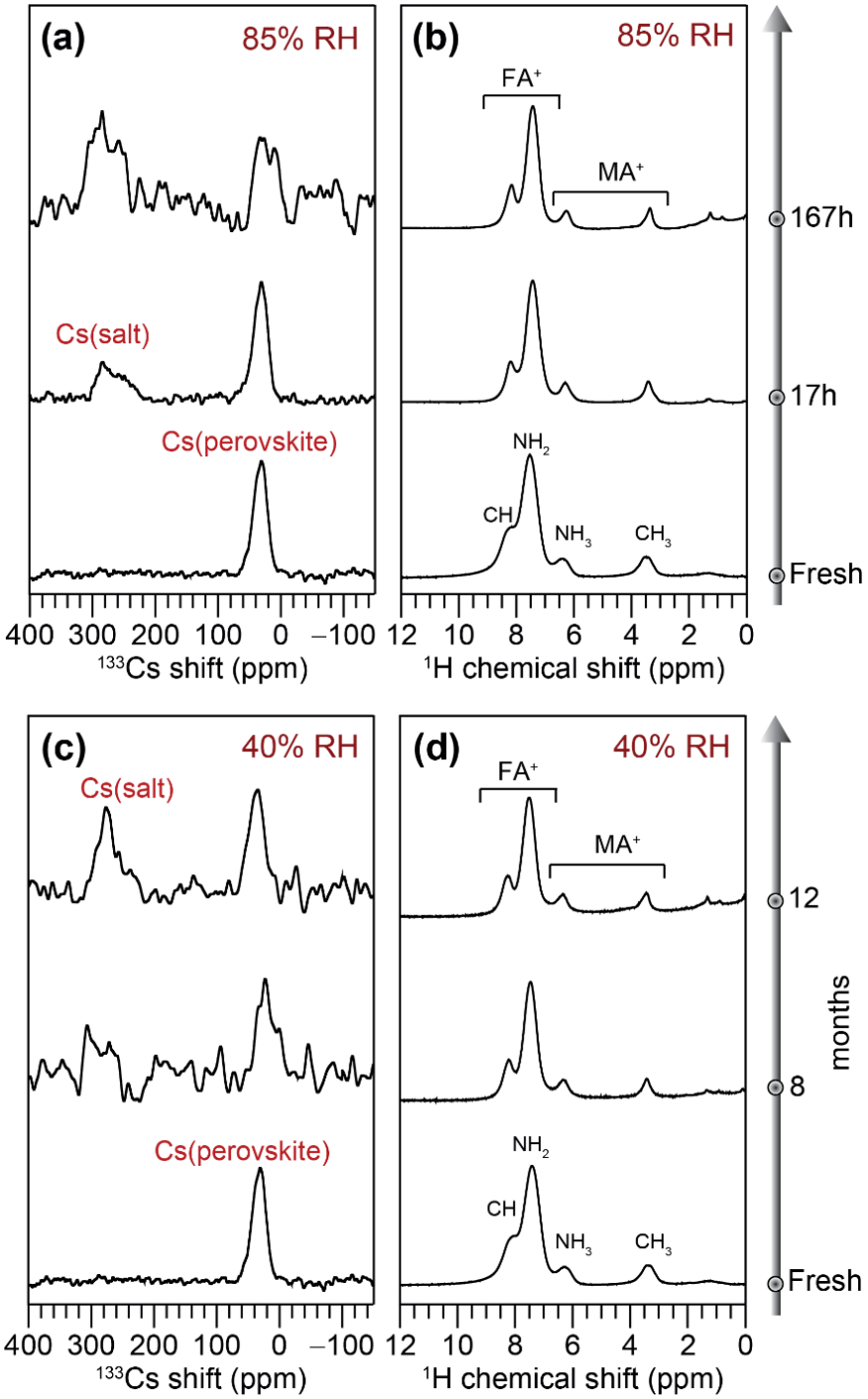


**Figure 7.** Solid-state 1D NMR spectra of CsMAFA powder scratched from the thin films deposited on the glass substrates. (a, c) $^{133}$Cs (104.9 MHz, 18.8 T) MAS and (b, d) $^{1}$H (800.1 MHz, 18.8 T) MAS spectra before and after exposure to moisture at (a, b) 85% and (c, d) 40% RH. All spectra were acquired at room temperature.

Likewise, the water vapor concentration is expected to play a significant role in governing the stability of the CsMAFA thin films. Upon exposing the CsMAFA material at 40% RH, an additional $^{133}Cs$ signal is observed at 278 ppm (Figure 7c) after 8 months (instead of 17 h for 85% RH). This signal is attributable to the formation of non-perovskite inorganic Cs compounds – identical to those observed in the case of CsMAFA at 85% RH, but these moieties are formed at a much slower rate owing to the lower RH. The 1D $^{1}H$ NMR spectrum of CsMAFA aged at 40% RH for up to a year (Figure 7d) is identical to that of CsMAFA exposed to 85% RH during 167 h. These results conclude that some of the $Cs^{+}$ cations remain in the perovskite framework, and the others tend to migrate out to form the non-perovskite structure even in the presence of a low concentration of water molecules. This raises a question regarding other A-site cations in the composition.

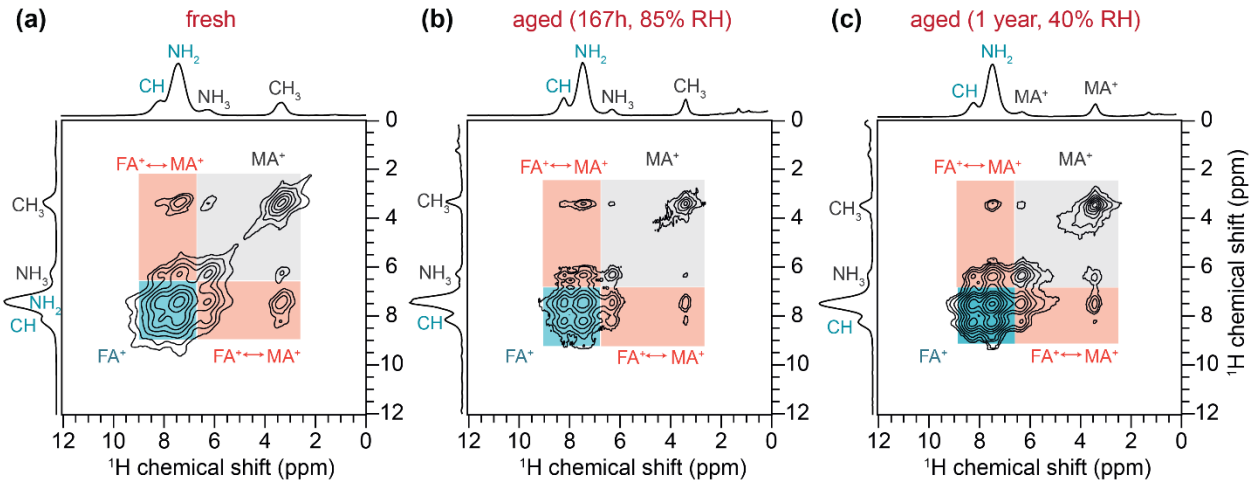


**Figure 8.** Solid-state 2D $^{1}H$-$^{1}H$ SD NMR spectrum of CsMAFA acquired with 500 ms mixing time for (a) pristine and after exposure to moisture for (b) 167h at 85% RH and (c) 1 year at 40% RH. Peaks correspond to $MA^{+}$, and $FA^{+}$ cations are color coded as depicted in the boxes.

In order to probe the spatial proximities between A-site organic cations in CsMAFA, we analyzed 2D $^{1}$H-$^{1}$H SD spectra acquired with 500 ms of mixing time before and after exposure to moisture. In the 2D SD spectrum of the fresh material (Figure 8a), the peaks depicted in the grey-shaded rectangle (3.4-6.6 ppm) correspond to $MA^{+}$ cations, and the 2D peaks in the cyan-shaded rectangle (7.4-8.6 ppm) correspond to the $FA^{+}$ moieties, respectively. Specifically, the 2D peaks highlighted in the orange-shaded rectangle indicate the intermolecular dipolar interactions between the $MA^{+}$ and $FA^{+}$ protons. For the aged CsMAFA, the 2D $^{1}$H-$^{1}$H SD spectrum (Figure 8b) showed identical cross-peaks but with less intensity suggesting that the exposure to moisture leads to the partial clustering of $MA^{+}$ and $FA^{+}$ cations.[92] It has been shown that the driving force for such local clustering of organic cations is the increased dynamical freedom, which lowers the free energy of the system.[92] However, the 2D SD spectrum acquired after exposure to moisture for 1 year aged at 40% RH leads to the cross-peaks with higher intensity (Figure 8c), further corroborating that the concentration of water molecules influences the degradation kinetics of CsMAFA thin films. Interestingly, the moisture-aged CsMAFA thin film did not show the signatures, irrespective of the aging conditions, corresponding to the formation of MAI or δ-$FAPbI_3$ phase that are among the degradation products of $MAPbI_3$ or $FAPbI_3$ materials.[77] This result is intriguing and calls for the further investigation of $FA^{+}$ and $MA^{+}$ cation stability in the CsMAFA formulation.

**Moisture-catalyzed transformative reactions and degradation products**.

Figure 9 summarizes the different reaction pathways and the intermediate species produced by the exposure of perovskite thin films to moisture at different relative humidity levels, as characterized by XRD and ssNMR techniques. These results indicate that the $MAPbI_3$ transforms into the solid solution of its hydrate, $PbI_2$, and MAI (Figure 9a) in the presence of a relatively high concentration of water vapor (85% RH), but the same material in the presence of low water vapor content (40%

RH) leads to an interconversion between $MAPbI_3$ and its monohydrate inhibiting the degradation reactions to complete. Therefore, the degradation pathways and the associated reaction kinetics depends strongly on the water vapor concentration in the air, which can be identified, distinguished and quantified (Figure 2) by $^1H$ MAS solid-state spectroscopy in conjunction with. In contrast to this, the defects passivated $MAPbI_3$.TPA(4mol.%) tends to undergo transformative reactions at a much slower rate than pristine $MAPbI_3$ even at high concentration of water vapor (Figure 9b), leading to enhanced moisture stability, although a minuscule concentration of MAI (~5%) is formed after exposure to moisture for over 3 days.[47,54] The longevity of this material is further enhanced in the presence of low water vapor concentration in the air (40% RH). Despite of the hygroscopic nature of TPAI, the strong affinity interactions between the $TPA^+$ and $MAPbI^3$ reduces the water ingression, enabling the longevity of this later against moisture, consistently with the enhanced stability in the solar cells.[47] Intriguingly, the FA-rich CsMAFA appears to be relatively more stable against moisture among the hybrid perovskite thin films analyzed in this study. However, some of the $Cs^+$ ions appear to migrate from the perovskite framework to form non-perovskite inorganic compounds (Figure 9c). The organic cations ($MA^+$, $FA^+$) tend to be part of the perovskite structure even after exposure to moisture for a prolonged duration of up to one year. This is particularly intriguing because the pristine $\alpha$-$FAPbI_3$,[77] $\alpha$-$CsPbI_3$,[93,94] and $MAPbI_3$[54] are unstable with respect to moisture, but their mixed cation CsMAFA is comparably more stable. Different affinity interactions between the A-site cations and inorganic lead halide octahedra leads to the different degradation reactions, and migration of A-site cations from the perovskite framework into the non-perovskite phases occurs in the presence of water molecules. Kinetics of these transformative and reconstructive reactions depends strongly on the concentration of water molecules in the vapor. We hypothesize that the A-site cation distribution, in addition to the other

factors such as mixed halides, plays a role in determining the moisture stability of triple cation formulation. However, a detailed understanding of cation mapping in this formulation using XRD and ssNMR techniques is less straightforward and necessitates further investigation.[92]

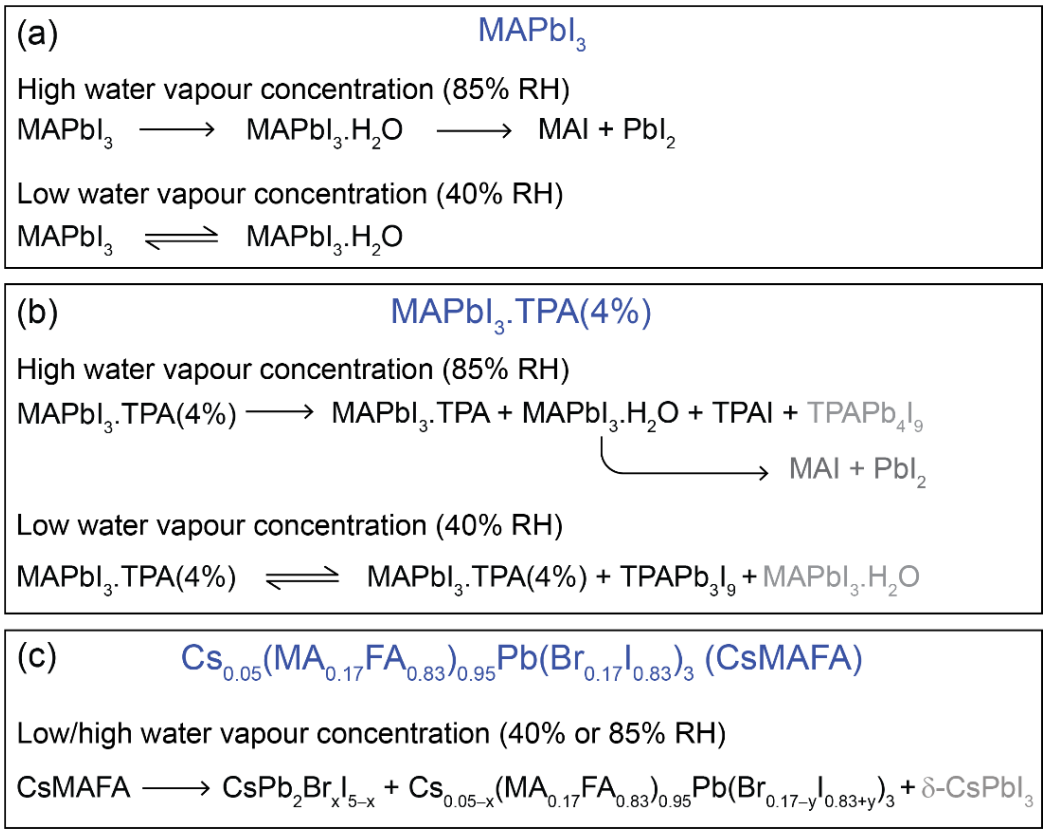


**Figure 9.** Proposed reaction degradation pathways of (a) $MAPbI_3$, (b) $MAPbI_3$.TPA (4 mol.%) and (c) CsMAFA thin films after exposure to different water vapor concentrations (85%/ 40% RH) based on this study.

Different degradation products of MA FA, and CsMAFA-based perovskites studied by different analytical techniques are summarized in Table 1. A broad spectrum of analytical techniques, including XRD and electron microscopy, are suitable for tracking the morphological changes in

the perovskite thin films under external stressors. Short-range probes such as ssNMR spectroscopy and other structural elucidation techniques are particularly important to correlate and complement the results obtained by long-range probes. In addition, *in situ* techniques with adequate spatial and temporal resolution need to be applied to gain insight into the structural changes in order to comprehensively understand the macroscopic physical performance of the PSCs devices. Morphological features resolved by the combination these techniques at different length scales are expected to provide path forward to characterize isolated thin films of perovskites and charge transport layers, and interfaces between them in stacked devices, in order to understand and compare the different powder conversation efficiencies exhibited perovskite solar cells. In particular, A-site cations have dramatic impact on the overall stability and phase behavior of 3D perovskite thin films. Mixed A-site cation and X-site anion alloys such as CsMAFA benefit from the adjustable tolerance factor in stabilizing the perovskite structure. The impact of A-site cations on the formation, phase behavior, stability and optoelectronic properties of 3D perovskites can be characterized by multitechnique approach. In addition, distribution of these A-site/X-site ions in the perovskite lattice also plays a role in governing (in)stability. Therefore, these methods and analyses is can be used to acquire deep new understandings of structure-stability-property relationships in perovskite photovoltaics.

**Table 1. Moisture-induced degradation products in hybrid perovskites as analyzed by different characterization techniques.**

| Material | Exposure to moisture | Byproducts formed | Characterization technique | Ref. |
|---|---|---|---|---|
| $MAPbI_3$ (thin-film) | 40% RH | $MAPbI_3.H_2O$ | ssNMR | This work |
| $MAPbI_3$ (thin-film) | 85% RH | $MAPbI_3.H_2O$, MAI | XRD, ssNMR | This work |
| $MAPbI_3$.TPA (thin film) | 40% RH | $MAPbI_3.H_2O$ | ssNMR | This work |
| $MAPbI_3$.TPA (thin film) | 85% RH | $TPAPb_4I_9$, MAI | XRD, ssNMR | This work |
| CsMAFA (thin-film) | 40% RH | δ-$CsPbI_3$, $CsPb_2Br_5$, $PbI_2$, $CsPb_2Br_xI_{5-x}$ | ssNMR, XRD | This work |
| CsMAFA (thin-film) | 85% RH | δ-$CsPbI_3$, $CsPb_2Br_5$, $PbI_2$ $CsPb_2Br_xI_{5-x}$ | ssNMR, XRD | This work |
| $MAPbI_3$ (polycrystalline) | 80% RH | $MAPbI_3.H_2O$ | ssNMR | 51 |
| $MAPbI_3$ (polycrystalline) | Aqueous solution | $MAPbI_3.H_2O$, $PbI_2$ | ssNMR | 51 |
| $MAPbI_3$ (polycrystalline) | Aqueous solution | $MAPbI_3.H_2O$ | XRD | 78 |

| | | | | |
|---|---|---|---|---|
| $MAPbI_3$ (polycrystalline) | Aqueous solution | $MA_4PbI_6.2H_2O$ | XRD | 95 |
| $MAPbI_3$ (thin-film) | 90% RH | $MA_4PbI_6.2H_2O$ | XRD | 96 |
| $MAPbI_3$ (thin-film) | Water vapor | $MA_4PbI_6.2H_2O$ | Grazing incidence X-ray diffraction | 97 |
| $MAPbI_3$ (thin-film) | 60% RH | $PbI_2$ | XRD | 98 |
| CsMAFA (thin-film) | 85% RH | $CsPb_2Br_5$, $Cs_{0.05-x}(MA_{0.17}FA_{0.83})_{0.95}Pb(Br_{0.17-2y}I_{0.83+2y})_3$ | TEM, XRD, ssNMR | 57 |
| $\alpha$-$FAPbI_3$ (thin film) | 85% RH | $\delta$-$FAPbI_3$ | FT-IR, AFM, XRD | 99 |
| $\alpha$-$FAPbI_3$ (polycrystalline) | 85% RH | $\delta$-$FAPbI_3$ | XRD, ssNMR | 77 |

## Conclusions

Understanding the transformative and cascading degradation reactions of hybrid perovskites is a crucially important factor in developing environmentally stable perovskite-based optoelectronic devices. This study provides molecular level insights into the different degradation pathways and the formation of byproducts, and how such reactions influence the long-term moisture stability and reaction kinetics for up to one year for $MAPbI_3$, $MAPbI_3$.TPA (4 mol%), and CsMAFA thin films. These degradation reactions occur by forming organic/inorganic and hybrid byproducts, and the equilibrium between the reactants and products depends on the concentration of water molecules and aging time, as analyzed by XRD and ssNMR techniques. For $MAPbI_3$, exposure to moisture (85% RH) leads to the formation of $MAPbI_3$ monohydrate, $PbI_2$, and MAI, whereby ssNMR spectroscopy aids in determining dilute organic degradation products that are challenging to detect using XRD techniques. The higher water concentration (85% RH) shifts the equilibrium towards the formation of byproducts, and the relatively low water vapor concertation (40% RH) leads to an equilibrium between the fresh material and its hydrates. As a result, the moisture stability of $MAPbI_3$ can be adjusted from a few hours to several months, depending on the aging condition. Surface defect passivation by $TPA^+$ cations impedes the moisture-induced degradation processes, however, prolonged exposure to a harshly humid condition (85% RH) triggers the degradation reactions. For CsMAFA, exposure to moisture leads to partial elimination of $Cs^+$ cations, but organic cations tend to preserve the perovskite structure even after exposure to moisture (45% RH) for over a year. These understandings and key results provide essential structural insights into the perovskite instability and the associated kinetics aspects, and thus expected to provide a guidance to the design of interfacial engineering in order to develop stable and efficient formulations for perovskite photovoltaics.

**Acknowledgements**

We thank Mercouri Kanatzidis and Michael Chabynic for insightful discussions. The financial support from EU Horizon 2020 research and innovation programme under the Marie Skłodowska-Curie grant no. 795091 is acknowledged. PR, OL, LD and MR are grateful to Région Hauts-de-France and University of Lille for the financial support. SSNMR experiments are conducted at high-field NMR facility in Lille, which is co-financed by IR INFRANALYTICS FR2054. MAAK and FS acknowledge financial support of Région Hauts-de-France and EDF of "Perovstab" project. JR and FS acknowledges financial support of the French ministry of education and research for PhD grant.

**Supporting Information**

Experimental details and acquisition parameters of 1D and 2D NMR spectra, SEM images and analysis of powder XRD patterns of pristine and defect passivated $MAPbI_3$ and $MAPbI_3$.TPA materials before and after exposure to moisture, and analysis of 2D $^{1}H$-$^{1}H$ correlation NMR spectra of these materials. In addition, indexed PXRD patterns of CsMAFA and different $CsPb_2Br_5$, $CsPb_2Br_xI_{5-x}$ (x= 1-5), and 1D $^{133}Cs$ MAS NMR spectra of $CsPb_2Br_xI_{5-x}$ (x= 1-5), CsI, $CsPbI_3$, $CsPbBr_3$ and CsMAFA compounds are presented.

**Conflicts of Interest**

Authors declare no conflict of interest

## References


(1) *Best Research-Cell Efficiency Chart | Photovoltaic Research | NREL*. www.nrel.gov/pv/cell-efficiency.html (accessed 2022-09-12).

(2) Jeong, J.; Kim, M.; Seo, J.; Lu, H.; Ahlawat, P.; Mishra, A.; Yang, Y.; Hope, M. A.; Eickemeyer, F. T.; Kim, M.; Yoon, Y. J.; Choi, I. W.; Darwich, B. P.; Choi, S. J.; Jo, Y.; Lee, J. H.; Walker, B.; Zakeeruddin, S. M.; Emsley, L.; Rothlisberger, U.; Hagfeldt, A.; Kim, D. S.; Grätzel, M.; Kim, J. Y. Pseudo-Halide Anion Engineering for α-$FAPbI_3$ Perovskite Solar Cells. *Nature* **2021**, *592*, 381–385.

(3) Min, H.; Lee, D. Y.; Kim, J.; Kim, G.; Lee, K. S.; Kim, J.; Paik, M. J.; Kim, Y. K.; Kim, K. S.; Kim, M. G.; Shin, T. J.; Il Seok, S. Perovskite Solar Cells with Atomically Coherent Interlayers on SnO2 Electrodes. *Nature* **2021**, *598*, 444–450.

(4) Kim, M.; Jeong, J.; Lu, H.; Lee, T. K.; Eickemeyer, F. T.; Liu, Y.; Choi, I. W.; Choi, S. J.; Jo, Y.; Kim, H. B.; Mo, S. I.; Kim, Y. K.; Lee, H.; An, N. G.; Cho, S.; Tress, W. R.; Zakeeruddin, S. M.; Hagfeldt, A.; Kim, J. Y.; Grätzel, M.; Kim, D. S. Conformal Quantum Dot-$SnO_2$ Layers as Electron Transporters for Efficient Perovskite Solar Cells. *Science* **2022**, *375*, 302–306.

(5) Ali, J.; Li, Y.; Gao, P.; Hao, T.; Song, J.; Zhang, Q.; Zhu, L.; Wang, J.; Feng, W.; Hu, H.; Liu, F. Interfacial and Structural Modifications in Perovskite Solar Cells. *Nanoscale* **2020**, *12*, 5719–5745.

(6) Hui, W.; Chao, L.; Lu, H.; Xia, F.; Wei, Q.; Su, Z.; Niu, T.; Tao, L.; Du, B.; Li, D.; Wang, Y.; Zuo, S.; Li, B.; Shi, W.; Ran, X.; Li, P.; Zhang, H.; Wu, Z.; Ran, C.; Song, L.; Xing, G.; Gao, X.; Zhang, J.; Xia, Y.; Chen, Y.; Huang, W. Stabilizing Black-Phase Formamidinium Perovskite Formation at Room Temperature and High Humidity. *Science* **2021**, *371*, 1359–1364.

(7) Park, B. wook; Kwon, H. W.; Lee, Y.; Lee, D. Y.; Kim, M. G.; Kim, G.; Kim, K. jeong; Kim, Y. K.; Im, J.; Shin, T. J.; Seok, S. Il. Stabilization of Formamidinium Lead Triiodide α-Phase with Isopropylammonium Chloride for Perovskite Solar Cells. *Nat. Energy* **2021**, *6*, 419–428.

(8) Saidaminov, M. I.; Kim, J.; Jain, A.; Quintero-Bermudez, R.; Tan, H.; Long, G.; Tan, F.; Johnston, A.; Zhao, Y.; Voznyy, O.; Sargent, E. H. Suppression of Atomic Vacancies via

Incorporation of Isovalent Small Ions to Increase the Stability of Halide Perovskite Solar Cells in Ambient Air. *Nat. Energy* **2018**, *3*, 648–654.

(9) Bryant, D.; Aristidou, N.; Pont, S.; Sanchez-Molina, I.; Chotchunangatchaval, T.; Wheeler, S.; Durrant, J. R.; Haque, S. A. Light and Oxygen Induced Degradation Limits the Operational Stability of Methylammonium Lead Triiodide Perovskite Solar Cells. *Energy Environ. Sci.* **2016**, *9*, 1655–1660.

(10) Ma, L.; Guo, D.; Li, M.; Wang, C.; Zhou, Z.; Zhao, X.; Zhang, F.; Ao, Z.; Nie, Z. Temperature-Dependent Thermal Decomposition Pathway of Organic-Inorganic Halide Perovskite Materials. *Chem. Mater.* **2019**, *31*, 8515–8522.

(11) Niu, G.; Guo, X.; Wang, L. Review of Recent Progress in Chemical Stability of Perovskite Solar Cells. *J. Mater. Chem. A* **2015**, *3*, 8970–8980.

(12) Futscher, M. H.; Lee, J. M.; McGovern, L.; Muscarella, L. A.; Wang, T.; Haider, M. I.; Fakharuddin, A.; Schmidt-Mende, L.; Ehrler, B. Quantification of Ion Migration in $CH_3NH_3PbI_3$ Perovskite Solar Cells by Transient Capacitance Measurements. *Mater. Horizons* **2019**, *6*, 1497–1503.

(13) Suchan, K.; Just, J.; Beblo, P.; Rehermann, C.; Merdasa, A.; Mainz, R.; Scheblykin, I. G.; Unger, E. Multi-Stage Phase-Segregation of Mixed Halide Perovskites under Illumination: A Quantitative Comparison of Experimental Observations and Thermodynamic Models. *Adv. Funct. Mater.* **2022**, 2206047.

(14) Boyd, C. C.; Cheacharoen, R.; Leijtens, T.; McGehee, M. D. Understanding Degradation Mechanisms and Improving Stability of Perovskite Photovoltaics. *Chem. Rev.* **2019**, *119*, 3418–3451.

(15) Kundu, S.; Kelly, T. L. In Situ Studies of the Degradation Mechanisms of Perovskite Solar Cells. *EcoMat* **2020**, *2*, e12025.

(16) Khenkin, M. V.; Katz, E. A.; Abate, A.; Bardizza, G.; Berry, J. J.; Brabec, C.; Brunetti, F.; Bulović, V.; Burlingame, Q.; Di Carlo, A.; Cheacharoen, R.; Cheng, Y. B.; Colsmann, A.; Cros, S.; Domanski, K.; Dusza, M.; Fell, C. J.; Forrest, S. R.; Galagan, Y.; Di Girolamo, D.; Grätzel, M.; Hagfeldt, A.; von Hauff, E.; Hoppe, H.; Kettle, J.; Köbler, H.; Leite, M. S.; Liu, S. (Frank); Loo, Y. L.; Luther, J. M.; Ma, C. Q.; Madsen, M.; Manceau, M.; Matheron, M.; McGehee, M.; Meitzner, R.; Nazeeruddin, M. K.; Nogueira, A. F.; Odabaşı, Ç.; Osherov, A.; Park, N. G.; Reese, M. O.; De Rossi, F.; Saliba, M.; Schubert, U. S.; Snaith,

H. J.; Stranks, S. D.; Tress, W.; Troshin, P. A.; Turkovic, V.; Veenstra, S.; Visoly-Fisher, I.; Walsh, A.; Watson, T.; Xie, H.; Yıldırım, R.; Zakeeruddin, S. M.; Zhu, K.; Lira-Cantu, M. Consensus Statement for Stability Assessment and Reporting for Perovskite Photovoltaics Based on ISOS Procedures. *Nat. Energy* **2020**, *5*, 35–49.

(17) Zhang, D.; Li, D.; Hu, Y.; Mei, A.; Han, H. Degradation Pathways in Perovskite Solar Cells and How to Meet International Standards. *Commun. Mater.* **2022**, *3*, 58.

(18) Lee, M. M.; Teuscher, J.; Miyasaka, T.; Murakami, T. N.; Snaith, H. J. Efficient Hybrid Solar Cells Based on Meso-Superstructured Organometal Halide Perovskites. *Science* **2012**, *338*, 643–647.

(19) Xing, G.; Mathews, N.; Sun, S.; Lim, S. S.; Lam, Y. M.; Graẗzel, M.; Mhaisalkar, S.; Sum, T. C. Long-Range Balanced Electron-and Hole-Transport Lengths in Organic-Inorganic $CH_3NH_3PbI_3$. *Science* **2013**, *342*, 344–347.

(20) Stranks, S. D.; Eperon, G. E.; Grancini, G.; Menelaou, C.; Alcocer, M. J. P.; Leijtens, T.; Herz, L. M.; Petrozza, A.; Snaith, H. J. Electron-Hole Diffusion Lengths Exceeding 1 Micrometer in an Organometal Trihalide Perovskite Absorber. *Science* **2013**, *342*, 341–344.

(21) Kim, M.; Lee, T. K.; Choi, I. W.; Choi, H. W.; Jo, Y.; Lee, J.; Kim, G. H.; Kwak, S. K.; Kim, D. S. Effects of Cation Size and Concentration of Cationic Chlorides on the Properties of Formamidinium Lead Iodide Based Perovskite Solar Cells. *Sustain. Energy Fuels* **2020**, *4*, 3753–3763.

(22) Mcmeekin, D. P.; Sadoughi, G.; Rehman, W.; Eperon, G. E.; Saliba, M.; Hörantner, M. T.; Haghighirad, A.; Sakai, N.; Korte, L.; Rech, B.; Johnston, M. B.; Herz, L. M.; Snaith, H. J. A Mixed-Cation Lead Mixed-Halide Perovskite Absorber for Tandem Solar Cells. *Science* **2016**, *351*, 151–155.

(23) Saliba, M.; Matsui, T.; Seo, J. Y.; Domanski, K.; Correa-Baena, J. P.; Nazeeruddin, M. K.; Zakeeruddin, S. M.; Tress, W.; Abate, A.; Hagfeldt, A.; Grätzel, M. Cesium-Containing Triple Cation Perovskite Solar Cells: Improved Stability, Reproducibility and High Efficiency. *Energy Environ. Sci.* **2016**, *9*, 1989–1997.

(24) Sutherland, B. R.; Sargent, E. H. Perovskite Photonic Sources. *Nat. Photonics* **2016**, *10*, 295–302.

(25) Zhou, Y.; Herz, L. M.; Jen, A. K. Y.; Saliba, M. Advances and Challenges in Understanding the Microscopic Structure–Property–Performance Relationship in Perovskite Solar Cells.

*Nat. Energy* **2022**, *7*, 794–807.

(26) Correa-Baena, J. P.; Saliba, M.; Buonassisi, T.; Grätzel, M.; Abate, A.; Tress, W.; Hagfeldt, A. Promises and Challenges of Perovskite Solar Cells. *Science* **2017**, *358*, 739–744.

(27) Hoke, E. T.; Slotcavage, D. J.; Dohner, E. R.; Bowring, A. R.; Karunadasa, H. I.; McGehee, M. D. Reversible Photo-Induced Trap Formation in Mixed-Halide Hybrid Perovskites for Photovoltaics. *Chem. Sci.* **2014**, *6*, 613–617.

(28) Slotcavage, D. J.; Karunadasa, H. I.; McGehee, M. D. Light-Induced Phase Segregation in Halide-Perovskite Absorbers. *ACS Energy Lett.* **2016**, *1*, 1199–1205.

(29) Brivio, F.; Caetano, C.; Walsh, A. Thermodynamic Origin of Photoinstability in the $CH_3NH_3Pb(I_{1-x}Br_x)_3$ Hybrid Halide Perovskite Alloy. *J. Phys. Chem. Lett.* **2016**, *7*, 1083–1087.

(30) Tsai, H.; Nie, W.; Blancon, J. C.; Stoumpos, C. C.; Asadpour, R.; Harutyunyan, B.; Neukirch, A. J.; Verduzco, R.; Crochet, J. J.; Tretiak, S.; Pedesseau, L.; Even, J.; Alam, M. A.; Gupta, G.; Lou, J.; Ajayan, P. M.; Bedzyk, M. J.; Kanatzidis, M. G.; Mohite, A. D. High-Efficiency Two-Dimensional Ruddlesden-Popper Perovskite Solar Cells. *Nature* **2016**, *536*, 312–317.

(31) Leyden, M. R.; Matsushima, T.; Qin, C.; Ruan, S.; Ye, H.; Adachi, C. Amplified Spontaneous Emission in Phenylethylammonium Methylammonium Lead Iodide Quasi-2D Perovskites. *Phys. Chem. Chem. Phys.* **2018**, *20*, 15030–15036.

(32) Grancini, G.; Roldán-Carmona, C.; Zimmermann, I.; Mosconi, E.; Lee, X.; Martineau, D.; Narbey, S.; Oswald, F.; De Angelis, F.; Graetzel, M.; Nazeeruddin, M. K. One-Year Stable Perovskite Solar Cells by 2D/3D Interface Engineering. *Nat. Commun.* **2017**, *8*, 15684.

(33) Stoumpos, C. C.; Cao, D. H.; Clark, D. J.; Young, J.; Rondinelli, J. M.; Jang, J. I.; Hupp, J. T.; Kanatzidis, M. G. Ruddlesden − Popper Hybrid Lead Iodide Perovskite 2D Homologous Semiconductors. *Chem. Mater.* **2016**, *28*, 2852–2867.

(34) Dahod, N. S.; Paritmongkol, W.; Stollmann, A.; Settens, C.; Zheng, S. L.; Tisdale, W. A. Melting Transitions of the Organic Subphase in Layered Two-Dimensional Halide Perovskites. *J. Phys. Chem. Lett.* **2019**, *10*, 2924–2930.

(35) Ke, W.; Mao, L.; Stoumpos, C. C.; Hoffman, J.; Spanopoulos, I.; Mohite, A. D.; Kanatzidis, M. G. Compositional and Solvent Engineering in Dion–Jacobson 2D Perovskites Boosts Solar Cell Efficiency and Stability. *Adv. Energy Mater.* **2019**, *9*, 1803384.

(36) Li, X.; Hoffman, J. M.; Kanatzidis, M. G. The 2D Halide Perovskite Rulebook: How the Spacer Influences Everything from the Structure to Optoelectronic Device Efficiency. *Chem. Rev.* **2021**, *121*, 2230–2291.

(37) Wang, R.; Xue, J.; Wang, K. L.; Wang, Z. K.; Luo, Y.; Fenning, D.; Xu, G.; Nuryyeva, S.; Huang, T.; Zhao, Y.; Yang, J. L.; Zhu, J.; Wang, M.; Tan, S.; Yavuz, I.; Houk, K. N.; Yang, Y. Constructive Molecular Configurations for Surface-Defect Passivation of Perovskite Photovoltaics. *Science* **2019**, *366*, 1509–1513.

(38) Zhao, Y.; Zhu, P.; Huang, S.; Tan, S.; Wang, M.; Wang, R.; Xue, J.; Han, T. H.; Lee, S. J.; Zhang, A.; Huang, T.; Cheng, P.; Meng, D.; Lee, J. W.; Marian, J.; Zhu, J.; Yang, Y. Molecular Interaction Regulates the Performance and Longevity of Defect Passivation for Metal Halide Perovskite Solar Cells. *J. Am. Chem. Soc.* **2020**, *142*, 20071–20079.

(39) Kim, M.; Kim, G. H.; Lee, T. K.; Choi, I. W.; Choi, H. W.; Jo, Y.; Yoon, Y. J.; Kim, J. W.; Lee, J.; Huh, D.; Lee, H.; Kwak, S. K.; Kim, J. Y.; Kim, D. S. Methylammonium Chloride Induces Intermediate Phase Stabilization for Efficient Perovskite Solar Cells. *Joule* **2019**, *3*, 2179–2192.

(40) Fu, L.; Li, H.; Wang, L.; Yin, R.; Li, B.; Yin, L. Defect Passivation Strategies in Perovskites for an Enhanced Photovoltaic Performance. *Energy Environ. Sci.* **2020**, *13*, 4017–4056.

(41) Krishna, A.; Zhang, H.; Zhou, Z.; Gallet, T.; Dankl, M.; Ouellette, O.; Eickemeyer, F. T.; Fu, F.; Sanchez, S.; Mensi, M.; Zakeeruddin, S. M.; Rothlisberger, U.; Reddy, G. N. M.; Redinger, A.; Grätzel, M.; Hagfeldt, A. Nanoscale Interfacial Engineering Enables Highly Stable and Efficient Perovskite Photovoltaics. *Energy Environ. Sci.* **2021**, *14*, 5552–5562.

(42) Wang, S.; Wang, A.; Deng, X.; Xie, L.; Xiao, A.; Li, C.; Xiang, Y.; Li, T.; Ding, L.; Hao, F. Lewis Acid/Base Approach for Efficacious Defect Passivation in Perovskite Solar Cells. *J. Mater. Chem. A* **2020**, *8*, 12201–12225.

(43) Kim, J.; Ho-Baillie, A.; Huang, S. Review of Novel Passivation Techniques for Efficient and Stable Perovskite Solar Cells. *Sol. RRL* **2019**, *3*, 1800302.

(44) Peng, Q.; Zheng, X.; Zhang, X.; You, S.; Li, L.; Zhao, Y.; Zhang, S.; Luo, L.; Zeng, H.; Li, X. Radical Molecular Modulator for High-Performance Perovskite Solar Cells. *Front. Chem.* **2020**, *8*, 825.

(45) Wu, T.; Li, X.; Qi, Y.; Zhang, Y.; Han, L. Defect Passivation for Perovskite Solar Cells: From Molecule Design to Device Performance. *ChemSusChem* **2021**, *14*, 4354–4376.

(46) Xia, J.; Liang, C.; Gu, H.; Mei, S.; Li, S.; Zhang, N.; Chen, S.; Cai, Y.; Xing, G. Surface Passivation Toward Efficient and Stable Perovskite Solar Cells. *Energy Environ. Mater.* **2022**. https://doi.org/10.1002/eem2.12296.

(47) Krishna, A.; Akhavan Kazemi, M. A.; Sliwa, M.; Reddy, G. N. M.; Delevoye, L.; Lafon, O.; Felten, A.; Do, M. T.; Gottis, S.; Sauvage, F. Defect Passivation via the Incorporation of Tetrapropylammonium Cation Leading to Stability Enhancement in Lead Halide Perovskite. *Adv. Funct. Mater.* **2020**, *30*, 1909737.

(48) Deretzis, I.; Alberti, A.; Pellegrino, G.; Smecca, E.; Giannazzo, F.; Sakai, N.; Miyasaka, T.; Magna, A. La. Atomistic Origins of $CH_3NH_3PbI_3$ Degradation to $PbI_2$ in Vacuum. *Appl. Phys. Lett* **2015**, *106*, 131904.

(49) Zhao, J.; Cai, B.; Luo, Z.; Dong, Y.; Zhang, Y.; Xu, H.; Hong, B.; Yang, Y.; Li, L.; Zhang, W.; Gao, C. Investigation of the Hydrolysis of Perovskite Organometallic Halide CH3NH3PbI3 in Humidity Environment. *Sci. Rep.* **2016**, *6*, 21976.

(50) Huang, J.; Tan, S.; Lund, P. D.; Zhou, H. Impact of $H_2O$ on Organic-Inorganic Hybrid Perovskite Solar Cells. *Energy Environ. Sci.* **2017**, *10*, 2284–2311.

(51) Askar, A. M.; Bernard, G. M.; Wiltshire, B.; Shankar, K.; Michaelis, V. K. Multinuclear Magnetic Resonance Tracking of Hydro, Thermal, and Hydrothermal Decomposition of $CH_3NH_3PbI_3$. *J. Phys. Chem. C* **2017**, *121*, 1013–1024.

(52) Juarez-Perez, E. J.; Ono, L. K.; Qi, Y. Thermal Degradation of Formamidinium Based Lead Halide Perovskites into Sym-Triazine and Hydrogen Cyanide Observed by Coupled Thermogravimetry-Mass Spectrometry Analysis. *J. Mater. Chem. A* **2019**, *7*, 16912–16919.

(53) Zheng, X.; Wu, C.; Jha, S. K.; Li, Z.; Zhu, K.; Priya, S. Improved Phase Stability of Formamidinium Lead Triiodide Perovskite by Strain Relaxation. *ACS Energy Lett.* **2016**, *1*, 1014–1020.

(54) Kazemi, M. A. A.; Raval, P.; Cherednichekno, K.; Chotard, J.-N.; Krishna, A.; Demortiere, A.; Reddy, G. N. M.; Sauvage, F. Molecular-Level Insight into Correlation between Surface Defects and Stability of Methylammonium Lead Halide Perovskite Under Controlled Humidity. *Small Methods* **2021**, *5*, 2000834.

(55) Meng, X.; Tian, X.; Zhang, S.; Zhou, J.; Zhang, Y.; Liu, Z.; Chen, W. In Situ Characterization for Understanding the Degradation in Perovskite Solar Cells. *Sol. RRL* **2022**, *6*, 2200280.

(56) Choi, J. I. J.; Khan, M. E.; Hawash, Z.; Kim, K. J.; Lee, H.; Ono, L. K.; Qi, Y.; Kim, Y. H.; Park, J. Y. Atomic-Scale View of Stability and Degradation of Single-Crystal $MAPbBr_3$ Surfaces. *J. Mater. Chem. A* **2019**, *7*, 20760–20766.

(57) Kazemi, M. A. A.; Folastre, N.; Raval, P.; Sliwa, M.; Marie, J.; Nsanzimana, V.; Golonu, S.; Demortiere, A.; Rousset, J.; Lafon, O.; Delevoye, L.; Reddy, G. N. M.; Sauvage, F. Moisture-Induced Non-Equilibrium Phase Segregation in Triple Cation Mixed Halide Perovskite Monitored by In Situ Characterization Techniques and Solid-State NMR. *Energy Environ. Mater.* **2021**. https://doi.org/10.1002/eem2.12335.

(58) Kazemi, M. A. A.; Jamali, A.; Sauvage, F. A Holistic Study on the Effect of Annealing Temperature and Time on $CH_3NH_3PbI_3$-Based Perovskite Solar Cell Characteristics. *Front. Energy Res.* **2021**, *9*, 1–10.

(59) Dahlman, C. J.; Kubicki, D. J.; Reddy, G. N. M. Interfaces in Metal Halide Perovskites Probed by Solid-State NMR Spectroscopy. *J. Mater. Chem. A* **2021**, *9*, 19206–19244.

(60) Kubicki, D. J.; Stranks, S. D.; Grey, C. P.; Emsley, L. NMR Spectroscopy Probes Microstructure, Dynamics and Doping of Metal Halide Perovskites. *Nat. Rev. Chem.* **2021**, *5*, 624–645.

(61) Sarkar, D.; Hooper, R. W.; Karmakar, A.; Bhattacharya, A.; Pominov, A.; Terskikh, V. V.; Michaelis, V. K. Metal Halide Perovskite and Perovskite-like Materials through the Lens of Ultra-Wideline $^{35}/^{37}$Cl NMR Spectroscopy. *ACS Mater. Lett.* **2022**, *4*, 1255–1263.

(62) Hooper, R. W.; Sarkar, D.; Michaelis, V. K. Bulk and Nanoscale Semiconducting Materials: Structural Advances Using Solid-State NMR Spectroscopy. *Curr. Opin. Colloid Interface Sci.* **2022**, *62*, 101631.

(63) Franssen, W. M. J.; Kentgens, A. P. M. Solid–State NMR of Hybrid Halide Perovskites. *Solid State Nucl. Magn. Reson.* **2019**, *100*, 36–44.

(64) Aebli, M.; Piveteau, L.; Nazarenko, O.; Benin, B. M.; Krieg, F.; Verel, R.; Kovalenko, M. V. Lead-Halide Scalar Couplings in $^{207}$Pb NMR of $APbX_3$ Perovskites (A = Cs, Methylammonium, Formamidinium; X = Cl, Br, I). *Sci. Rep.* **2020**, *10*, 8229.

(65) Hanrahan, M. P.; Men, L.; Rosales, B. A.; Vela, J.; Rossini, A. J. Sensitivity-Enhanced $^{207}$Pb Solid-State NMR Spectroscopy for the Rapid, Non-Destructive Characterization of Organolead Halide Perovskites. *Chem. Mater.* **2018**, *30*, 7005–7015.

(66) Rosales, B. A.; Men, L.; Cady, S. D.; Hanrahan, M. P.; Rossini, A. J.; Vela, J. Persistent

Dopants and Phase Segregation in Organolead Mixed-Halide Perovskites. *Chem. Mater.* **2016**, *28*, 6848–6859.

(67) Franssen, W. M. J.; Van Es, S. G. D.; Dervişoğlu, R.; De Wijs, G. A.; Kentgens, A. P. M. Symmetry, Dynamics, and Defects in Methylammonium Lead Halide Perovskites. *J. Phys. Chem. Lett.* **2017**, *8*, 61–66.

(68) Mishra, A.; Hope, M. A.; Almalki, M.; Pfeifer, L.; Zakeeruddin, S. M.; Grätzel, M.; Emsley, L. Dynamic Nuclear Polarization Enables NMR of Surface Passivating Agents on Hybrid Perovskite Thin Films. *J. Am. Chem. Soc.* **2022**, *144*, 15175–15184.

(69) Piveteau, L.; Morad, V.; Kovalenko, M. V. Solid-State NMR and NQR Spectroscopy of Lead-Halide Perovskite Materials. *J. Am. Chem. Soc.* **2020**, *142*, 19413–19437.

(70) Dahlman, C. J.; Kennard, R. M.; Paluch, P.; Venkatesan, N. R.; Chabinyc, M. L.; Reddy, G. N. M. Dynamic Motion of Organic Spacer Cations in Ruddlesden–Popper Lead Iodide Perovskites Probed by Solid-State NMR Spectroscopy. *Chem. Mater.* **2021**, *33*, 642–656.

(71) Lee, J.; Lee, W.; Kang, K.; Lee, T.; Lee, S. K. Layer-by-Layer Structural Identification of 2D Ruddlesden–Popper Hybrid Lead Iodide Perovskites by Solid-State NMR Spectroscopy. *Chem. Mater.* **2021**, *33*, 370–377.

(72) Kubicki, D. J.; Prochowicz, D.; Salager, E.; Rakhmatullin, A.; Grey, C. P.; Emsley, L.; Stranks, S. D. Local Structure and Dynamics in Methylammonium, Formamidinium, and Cesium Tin(II) Mixed-Halide Perovskites from Sn Solid-State NMR. *J. Am. Chem. Soc.* **2020**, *142*, 7813–7826.

(73) Roiland, C.; Trippé-Allard, G.; Jemli, K.; Alonso, B.; Ameline, J. C.; Gautier, R.; Bataille, T.; Le Pollès, L.; Deleporte, E.; Even, J.; Katan, C. Multinuclear NMR as a Tool for Studying Local Order and Dynamics in $CH_3NH_3PbX_3$ (X = Cl, Br, I) Hybrid Perovskites. *Phys. Chem. Chem. Phys.* **2016**, *18*, 27133–27142.

(74) Dučinskas, A.; Kim, G. Y.; Moia, D.; Senocrate, A.; Wang, Y.-R.; Hope, M. A.; Mishra, A.; Kubicki, D. J.; Siczek, M.; Bury, W.; Schneeberger, T.; Emsley, L.; Milić, J. V.; Maier, J.; Grätzel, M. Unravelling the Behavior of Dion–Jacobson Layered Hybrid Perovskites in Humid Environments. *ACS Energy Lett.* **2021**, *6*, 337–344.

(75) Luginbuhl, B. R.; Raval, P.; Pawlak, T.; Du, Z.; Wang, T.; Kupgan, G.; Schopp, N.; Chae, S.; Yoon, S.; Yi, A.; Kim, H. J.; Coropceanu, V.; Brédas, J.-L.; Nguyen, T.-Q.; Reddy, G. N. M. Resolving Atomic-Scale Interactions in Nonfullerene Acceptor Organic Solar Cells

with Solid-State NMR Spectroscopy, Crystallographic Modelling, and Molecular Dynamics Simulations. *Adv. Mater.* **2022**, *34*, 2105943.

(76) Leguy, A. M. A.; Hu, Y.; Campoy-Quiles, M.; Alonso, M. I.; Weber, O. J.; Azarhoosh, P.; Van Schilfgaarde, M.; Weller, M. T.; Bein, T.; Nelson, J.; Docampo, P.; Barnes, P. R. F. Reversible Hydration of $CH_3NH_3PbI_3$ in Films, Single Crystals, and Solar Cells. *Chem. Mater.* **2015**, *27*, 3397–3407.

(77) Raval, P.; Kennard, R. M.; Vasileiadou, E. S.; Dahlman, C. J.; Spanopoulos, I.; Chabinyc, M. L.; Kanatzidis, M.; Reddy, G. N. M. Understanding Instability in Formamidinium Lead Halide Perovskites: Kinetics of Transformative Reactions at Grain and Subgrain Boundaries. *ACS Energy Lett.* **2022**, *7*, 1534–1543.

(78) Poglitsch, A.; Weber, D. Dynamic Disorder in Methylammoniumtrihalogenoplumbates (II) Observed by Millimeterwave Spectroscopy. *J. Chem. Phys.* **1987**, *87*, 6373–6378.

(79) Wang, B.; Chen, T. Exceptionally Stable $CH_3NH_3PbI_3$ Films in Moderate Humid Environmental Condition. *Adv. Sci.* **2015**, *3*, 1500262.

(80) Degani, M.; An, Q.; Albaladejo-Siguan, M.; Hofstetter, Y. J.; Cho, C.; Paulus, F.; Grancini, G.; Vaynzof, Y. 23.7% Efficient Inverted Perovskite Solar Cells by Dual Interfacial Modification. *Sci. Adv.* **2021**, *7*, 7930.

(81) Al-Ashouri, A.; Köhnen, E.; Li, B.; Magomedov, A.; Hempel, H.; Caprioglio, P.; Márquez, J. A.; Vilches, A. B. M.; Kasparavicius, E.; Smith, J. A.; Phung, N.; Menzel, D.; Grischek, M.; Kegelmann, L.; Skroblin, D.; Gollwitzer, C.; Malinauskas, T.; Jošt, M.; Matič, G.; Rech, B.; Schlatmann, R.; Topič, M.; Korte, L.; Abate, A.; Stannowski, B.; Neher, D.; Stolterfoht, M.; Unold, T.; Getautis, V.; Albrecht, S. Monolithic Perovskite/Silicon Tandem Solar Cell with >29% Efficiency by Enhanced Hole Extraction. *Science* **2020**, *370*, 1300–1309.

(82) Lee, J.-W.; Kim, D.-H.; Kim, H.-S.; Seo, S.-W.; Cho, S. M.; Park, N.-G. Formamidinium and Cesium Hybridization for Photo- and Moisture-Stable Perovskite Solar Cell. *Adv. Energy Mater.* **2015**, *5*, 1501310.

(83) Tan, W.; Bowring, A. R.; Meng, A. C.; McGehee, M. D.; McIntyre, P. C. Thermal Stability of Mixed Cation Metal Halide Perovskites in Air. *ACS Appl. Mater. Interfaces* **2018**, *10*, 5485–5491.

(84) Landi, N.; Maurina, E.; Marongiu, D.; Simbula, A.; Borsacchi, S.; Calucci, L.; Saba, M.; Carignani, E.; Geppi, M. Solid-State Nuclear Magnetic Resonance of Triple-Cation Mixed-

Halide Perovskites. *J. Phys. Chem. Lett.* **2022**, *13*, 9517–9525.

(85) Karmakar, A.; Dodd, M. S.; Zhang, X.; Oakley, M. S.; Klobukowski, M.; Michaelis, V. K. Mechanochemical Synthesis of 0D and 3D Cesium Lead Mixed Halide Perovskites. *Chem. Commun.* **2019**, *55*, 5079–5082.

(86) Wang, K. H.; Wu, L.; Li, L.; Yao, H. Bin; Qian, H. S.; Yu, S. H. Large-Scale Synthesis of Highly Luminescent Perovskite-Related $CsPb_2Br_5$ Nanoplatelets and Their Fast Anion Exchange. *Angew. Chemie Int. Ed.* **2016**, *55*, 8328–8332.

(87) Ruan, L.; Shen, W.; Wang, A.; Xiang, A.; Deng, Z. Alkyl-Thiol Ligand-Induced Shape- and Crystalline Phase-Controlled Synthesis of Stable Perovskite-Related $CsPb_2Br_5$ Nanocrystals at Room Temperature. *J. Phys. Chem. Lett.* **2017**, *8*, 3853–3860.

(88) Huang, Z. P.; Ma, B.; Wang, H.; Li, N.; Liu, R. T.; Zhang, Z. Q.; Zhang, X. D.; Zhao, J. H.; Zheng, P. Z.; Wang, Q.; Zhang, H. L. In Situ Growth of 3D/2D ($CsPbBr_3$/$CsPb_2Br_5$) Perovskite Heterojunctions toward Optoelectronic Devices. *J. Phys. Chem. Lett.* **2020**, *11*, 6007–6015.

(89) Lin, C.; Liu, L.; Xu, J.; Fang, F.; Jiang, K.; Liu, Z.; Wang, Y.; Chen, F.; Yao, H. Facile Synthesis of a Dual-Phase $CsPbBr_3$–$CsPb_2Br_5$ Single Crystal and Its Photoelectric Performance. *RSC Adv.* **2020**, *10*, 20745–20752.

(90) Li, M.; Peng, S.; Fang, S.; Gong, Y.; Yang, D.; Bu, K.; Liu, B.; Luo, H.; Guo, S.; Li, J.; Wang, H.; Liu, Y.; Jiang, S.; Lin, C.; Lü, X. Synthesis of Two-Dimensional $CsPb_2X_5$ (X = Br and I) with a Stable Structure and Tunable Bandgap by $CsPbX_3$ Phase Separation. *J. Phys. Chem. Lett.* **2022**, *13*, 2555–2562.

(91) Karmakar, A.; Bhattacharya, A.; Sarkar, D.; Bernard, G. M.; Mar, A.; Michaelis, V. K. Influence of Hidden Halogen Mobility on Local Structure of $CsSn(Cl_{1-x}Br_x)_3$ Mixed-Halide Perovskites by Solid-State NMR. *Chem. Sci.* **2021**, *12*, 3253–3263.

(92) Grüninger, H.; Bokdam, M.; Leupold, N.; Tinnemans, P.; Moos, R.; De Wijs, G. A.; Panzer, F.; Kentgens, A. P. M. Microscopic (Dis)Order and Dynamics of Cations in Mixed FA/MA Lead Halide Perovskites. *J. Phys. Chem. C* **2021**, *125*, 1742–1753.

(93) Moller, C. K. N. The Structure of Caesium Plumbo Iodide CsPbI3. *Mat. Fys. Medd. Dan. Vid. Selsk.* **1959**, *32*, 1.

(94) Stoumpos, C. C.; Malliakas, C. D.; Kanatzidis, M. G. Semiconducting Tin and Lead Iodide Perovskites with Organic Cations: Phase Transitions, High Mobilities, and near-Infrared

Photoluminescent Properties. *Inorg. Chem.* **2013**, *52*, 9019–9038.

(95) Vincent, B. R.; Robertson, K. N.; Cameron, T. S.; Knop, O. Alkylammonium Lead Halides. Part 1. Isolated $PbI_6^{4-}$ Ions in $(CH_3NH_3)_4PbI_6 \cdot 2H_2O$. *Can. J. Chem.* **1987**, *65*, 1042–1046.

(96) Christians, J. A.; Miranda Herrera, P. A.; Kamat, P. V. Transformation of the Excited State and Photovoltaic Efficiency of $CH_3NH_3PbI_3$ Perovskite upon Controlled Exposure to Humidified Air. *J. Am. Chem. Soc.* **2015**, *137*, 1530–1538.

(97) Yang, J.; Siempelkamp, B. D.; Liu, D.; Kelly, T. L. Investigation of $CH_3NH_3PbI_3$ Degradation Rates and Mechanisms in Controlled Humidity Environments Using in Situ Techniques. *ACS Nano* **2015**, *9*, 1955–1963.

(98) Niu, G.; Li, W.; Meng, F.; Wang, L.; Dong, H.; Qiu, Y. Study on the Stability of $CH_3NH_3PbI_3$ Films and the Effect of Post-Modification by Aluminum Oxide in All-Solid-State Hybrid Solar Cells. *J. Mater. Chem. A* **2014**, *2*, 705–710.

(99) Ho, K.; Wei, M.; Sargent, E. H.; Walker, G. C. Grain Transformation and Degradation Mechanism of Formamidinium and Cesium Lead Iodide Perovskite under Humidity and Light. *ACS Energy Lett.* **2021**, *6*, 934–940.